2011

Detecting Improvised Explosive Devices Via Forward Looking Ground Penetrating Radar

Will Woods
Bucknell University

Follow this and additional works at: https://digitalcommons.bucknell.edu/honors_theses

DETECTING IMPROVISED EXPLOSIVE DEVICES VIA FORWARD LOOKING GROUND

PENETRATING RADAR

by

William W. Woods

A Proposal Submitted to the Honors Council

For Honors in Electrical Engineering

2 May 2011

Approved by:

_____

Advisor: David Kelley

_____

Department Chairperson: David Kelley

Acknowledgments

I owe a sincere debt of gratitude to Professor David Kelley. His infinite patience, unfaltering willingness to share knowledge and resources, and silent forgiveness of my many morning class absences helped guide me to a place where I was able to simulate and write (and even understand!) what follows. Professor Rob Jacob's generous invitation to attend his Geology lectures granted me a new and valuable perspective on the fundamentals of GPR; this paper would be less without it. I extend my most genuine appreciation to every professor who has invested his or her time in me. Thank you.

Table of Contents

List of Tables

List of Figures

Abstract

Forward-looking ground penetrating radar shows promise for detection of improvised explosive devices in active war zones. Because of certain insurmountable physical limitations, post-processing algorithm development is the most popular research topic in this field. One such investigative avenue explores the worthiness of frequency analysis during data post-processing. Using the finite difference time domain numerical method, simulations are run to test both mine and clutter frequency response. Mines are found to respond strongest at low frequencies and cause periodic changes in ground penetrating radar frequency results. These results are called into question, however, when clutter, a phenomenon generally known to be random, is also found to cause periodic frequency effects. Possible causes, including simulation inaccuracy, are considered. Although the clutter models used are found to be inadequately random, specular reflections of differing periodicity are found to return from both the mine and the ground. The presence of these specular reflections offers a potential alternative method of determining a mine's presence.

Chapter 1: Introduction and Literature Review

Research into the detection of buried explosives has recently experienced a resurgence of interest and activity. Though landmine removal in abandoned war zones has already been deeply explored, recent conflicts in Afghanistan and Iraq have revealed a new buried explosive threat, the improvised explosive device (IED), also known as the roadside bomb. Combatants primarily use IEDs to attack moving vehicles such as humvees, personnel carriers, supply trucks and tanks. Because they utilize IEDs in active war zones, dangerous conditions limit the time, tools and manpower available to neutralize them. As a consequence, previously developed techniques used to detect landmines in inactive war zones are insufficient to counteract the IED.

One method of landmine detection employs ground penetrating radar (GPR) to detect unexploded ordinance (UXO). GPR systems direct their radar energy straight down into the ground (Fig. 1.1); as a result, a downward looking GPR system is most often used to locate targets in the subsurface directly beneath it. [1]
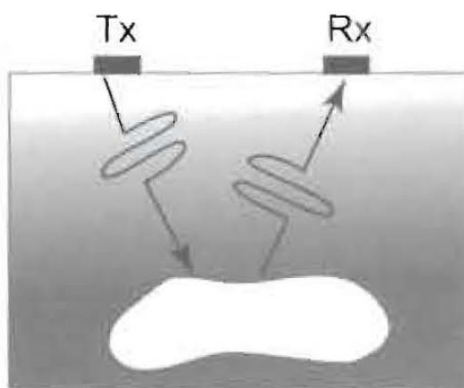
Figure 1.1. Basic GPR system.

In addition, GPR often touches the ground's surface when used for experiments not involving explosives. Niitek, a small engineering firm based in Sterling, Virginia, developed the

Husky Mounted Detection System (HMDS) to help explosive ordinance disposal teams detect and disarm IEDs. Though HMDS is large and robust, it moves slowly and is only capable of identifying dangers beneath its radar boom. It is not cost effective to place such expensive technology directly in the blast zone of an IED.

A better approach to IED detection with GPR is vehicle mounted forward-looking ground penetrating radar (FLGPR). FLGPR incorporates an antenna array that directs electromagnetic energy forward, at some angle below horizontal, rather than straight down (Fig. 1.2). This technique illuminates a swath of ground at some location downrange from the antenna array, and thus allows the GPR to be placed a safe distance from the target.

As recently as 2010, researchers working under the US Army's Night Vision and Electronic Sensors Directorate published their work exploring the use of an ultra – wideband FLGPR system to detect buried explosives. This system, known as ALARIC, uses a 0.3 – 3 GHz impulse radar to explore the ground subsurface. Study of this system is primarily for military purposes, exploring modularity and combat effectiveness. Preliminary results published in [2] suggest that the ALARIC system is capable of detecting buried metallic targets.

Researchers at the University of Hawaii published a comprehensive study of the feasibility of IED detection with FLGPR [3]. Their research investigates the presence of natural resonance frequency and polarization features in FLGPR results. They conclude that both natural resonances and polarization features are present and detectable with an FLGPR system, and recommend them as features of interest in future FLGPR detection algorithms. Such research establishes the feasibility of using FLGPR as a tool to detect IEDs.

The stand-off capability of FLGPR is, however, offset by a significant weakness; forward looking systems suffer from greatly diminished return energy. As a result it is very difficult to extract meaningful results from FLGPR data. Due to the physical nature of this limitation,

explained more thoroughly in Chapter 2, research typically focuses on developing algorithms

capable of differentiating between unwanted signal clutter and desired target returns.
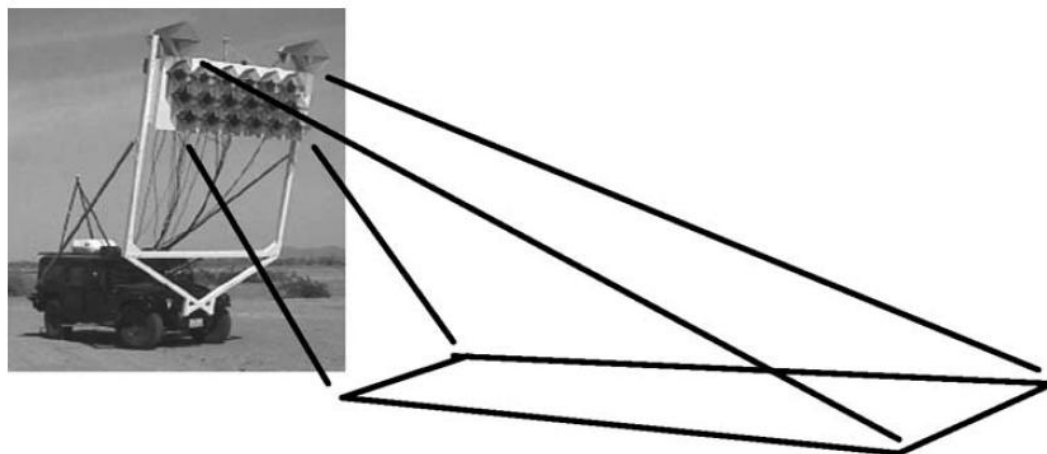
Figure 1.2. Experimental FLGPR system by SRI International. [5]

In particular, researchers in [4] investigate several different time domain analysis

techniques to help identify and characterize electromagnetic scattering from targets and clutter.

They apply their new techniques to experimental FLGPR data provided by the Stanford Research

Institute (SRI) and show increased detection rates over conventional identification methods. They

continue the march forward in time domain GPR post-processing, exploring new mathematical

methods of analyzing and interpreting temporal data.

While most algorithms manipulate time domain information from ultra wideband (UWB)

radar systems, however, [5] suggests a processing technique that analyzes frequency domain data

as well. Their results suggest that frequency domain results can aid in discrimination between a

target and surrounding clutter. They found that, of a 0.8 – 2.8 GHz bandwidth radar frequency

range, frequency analysis of the 0.75 – 1.35 GHz energy returns yielded the lowest false alarm

rate of all bandwidths analyzed. Thus frequency content can be used as an additional classifier in

FLGPR detection algorithms.

Other frequency domain work explores the idea of energy density spectrum (EDS). EDS is an object's frequency domain response to incident electromagnetic energy. It is, in essence, a unique electromagnetic signature that scatters from a target subjected to incident radiation. Results from [6] establish the presence of EDS signatures unique to buried landmines and propose incorporating EDS detection techniques into GPR post-processing algorithms. Much like the conclusions drawn in [5], these results encourage further investigation of the spectral response of buried explosives.

This paper explores spectral signal to clutter ratio using the finite difference time domain (FDTD) numerical analysis method. In particular the software package XFdtd 7, by Remcom Inc., uses FDTD to create a computerized electromagnetics simulation environment. Using this software, a highly directional antenna known as the Vivaldi horn simulates the FLGPR transmit antenna. Different ideal and cluttered cases are explored with and without a buried IED; the resulting simulation pairs with and without targets are compared in order to find frequency ranges most likely to indicate the presence of hidden explosives. Conversely, frequency bands that significantly scatter from clutter are also noted. In this way, certain lower frequency subbands within commonly used UWB radars are found to indicate the presence of buried explosives. Identification of such subbands aids in the exploration of frequency based classifiers in post processing algorithms such as those found in [5].

Scientists often use FDTD to explore GPR related problems. In 2006 researchers from the Center for Subsurface Sensing & Imaging Systems published their FDTD simulations [7] exploring methods of reducing the impact of clutter on GPR measurements. They investigated the effect of soaking a ground site with water before taking GPR measurements. They found that, as long as the ground is uniformly soaked, the greater contrast provided by the moisture improves one's ability to identify buried objects. They also found, however, that non-uniform moisture

distribution muddles GPR measurements, rendering them useless. They present their results as vibrant graphs of the output of their FDTD simulations.

Dr. Chi Chih Chen [8] from the University of Ohio utilized FDTD to determine the presence of lateral waves in FLGPR measurements. In this case, lateral waves were found to travel near the surface of an interface faster than the rest of the energy propagating in the ground. FDTD has also been used by Italian researchers to compare experimental GPR results to their expected theoretical counterparts [9]. They conclude their work with a proposal that the combination of theoretical FDTD GPR results with experimental GPR measurements may increase the overall accuracy of a GPR system. This work was published in 2010, and continues to this day; there is much GPR and FLGPR research that utilizes the powerful FDTD simulation method.

This paper is organized as follows. Chapter 2 presents the electromagnetic theory and limitations that apply to FLGPR while Chapter 3 describes the FDTD method. Chapter 4 details the simulation experiments performed and Chapter 5 analyzes their results. Chapter 6 concludes the paper and suggests future work in the topics of FLGPR and IED detection.

Chapter 2: Electromagnetic Theory and Limitations

Ground penetrating radar employs electromagnetic radiation to gather information at a distance. Specifically, a GPR system radiates energy towards a target and collects that which is reflected back. Due to the relatively short distances between a transmit antenna array and target, reflected energy is most often measured by a separate receive antenna, known as a receiver. The return signal measured at the receiver is analyzed during the post-processing phase; it is at this point that meaningful information is gleaned from GPR measurements. Current FLGPR systems use synthetic aperture radar (SAR), an important radar technique whose explanation lies beyond the scope of this paper.

2.1. Electromagnetic Properties of Materials

GPR measurements send electromagnetic energy through media as diverse as air, grass, soil, sand, rock and water. The electromagnetic parameters of each material affect a waves' condition as it propagates forward. Polarization, attenuation and speed are just a few of the wave characteristics affected by the electromagnetic characteristics of a medium. The three main parameters of concern are permittivity (ε), permeability (μ) and electrical conductivity (σ) [10].

Permittivity describes a material's response to electric fields within its volume. The permittivity of free space ε_0, otherwise known as vacuum permittivity, is approximately 8.854 x 10^{-12} F/m (Farads per meter). The permittivity of media besides free space is defined by relative permittivity ε_r, a unitless constant by which ε_0 is multiplied to determine permittivity in F/m. Relative permittivity and dielectric constant are terms used interchangeably throughout this paper.

Permeability is a measure of a material's response to magnetic flux within its volume. Iron, for example, with an extremely large permeability, is an excellent material for establishing

and transmitting magnetic flux. The permeability of free space μ_0, otherwise known as vacuum permeability, is $4\pi \times 10^{-7}$ H/m (Henries per meter). Relative permeability μ_r describes the permeability of materials as a factor of μ_0.

Electrical conductivity defines a material's ability to permit the flow of electric current within its volume. A good conductor like copper, which freely allows electron flow, has extremely high conductivity, while poor conductors like Teflon exhibit low conductivity values. Conductivity is measured in S/m (Siemens per meter).

A wealth of high accuracy constitutive parameter values for different materials can be found in most electromagnetics textbooks. These values are used in the simulations described later in order to accurately model and test environments of interest.

2.2. Wave Propagation and Attenuation

After a GPR broadcast antenna emits an electromagnetic wave, that wave must propagate through a variety of media in order to reach its target. The electrical parameters outlined above determine the effect each medium has on a wave's energy. Wave propagation is best explained in two separate stages. First, the ideal lossless case is analyzed. Following that, lossy media is discussed by adding a finite conductivity to the propagation analysis. The electromagnetic energy described in the following analysis is assumed to be a uniform plane wave; such an assumption is reasonable for purposes here. Unless specified otherwise, Chapter 7 of [10] provides full derivations and figures for the following discussions.

For a linear, isotropic homogeneous medium with scalar ε, σ and μ, electromagnetic waves obey Maxwell's Equations, shown below

$$\nabla \cdot \boldsymbol{E} = \frac{\rho}{\varepsilon_0},$$

(2.1)

$$\nabla \times \boldsymbol{E} = -j\omega\mu\boldsymbol{H}, \tag{2.2}$$

$$\nabla \cdot \boldsymbol{H} = 0, \tag{2.3}$$

$$\nabla \times \boldsymbol{H} = \boldsymbol{J} + j\omega\varepsilon\boldsymbol{E}. \tag{2.4}$$

Here $\boldsymbol{E}$ is electric field in V/m (Volts per meter), ρ is charge density in C/m^3, ω is radian frequency in radians per second, $\boldsymbol{H}$ is magnetic field intensity in A/m (Amperes per meter) and $\boldsymbol{J}$ is current density in A/m^2.

Because wave propagation here is assumed to be through charge free media, or media contaning no excess charge, $\boldsymbol{J}$ and ρ are set equal to 0. At this point, Maxwell's equations are solved to obtain electric and magnetic intensity field wave equations

$$\nabla^2 \boldsymbol{E} - \gamma^2 \boldsymbol{E} = 0, \tag{2.5}$$

$$\nabla^2 \boldsymbol{H} - \gamma^2 \boldsymbol{H} = 0. \tag{2.6}$$

The propagation constant γ is defined by,

$$\gamma^2 = -\omega^2\mu\varepsilon. \tag{2.7}$$

In the case of propagation through a lossless material, or a material for which σ = 0, a plane wave experiences no attenuation. Solutions to Equations (2.5) and (2.6) show that no component of the electric or magnetic fields lies in the direction of propagation. Also, a plane wave in certain lossy and lossless media can be characterized as a transverse electromagnetic (TEM) wave because the electric and magnetic fields are perpendicular to one another as well as to the direction of propagation $\hat{k}$ (Fig. 2.1).
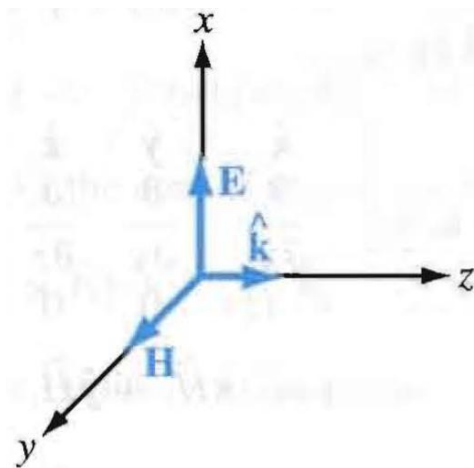
Figure 2.1. TEM wave direction vectors. [10]

Further analysis shows that in the case of both lossless and lossy materials, the wavelength, in meters, of an electromagnetic wave is defined below, where f is frequency in Hz, c is the speed of light in free space (approximately 2.997 x 10^8 m/s), v_p is the wave's propagation velocity in the medium and $\mu = \mu_0$.

$$\lambda = \frac{c}{f\sqrt{\varepsilon_r}} = \frac{v_p}{f} \tag{2.8}$$

When a plane wave travels through a lossy material with non-zero conductivity, it undergoes attenuation (Fig. 2.2) defined by,

$$|E(z)| = |E_0|e^{-\alpha z} \tag{2.9}$$
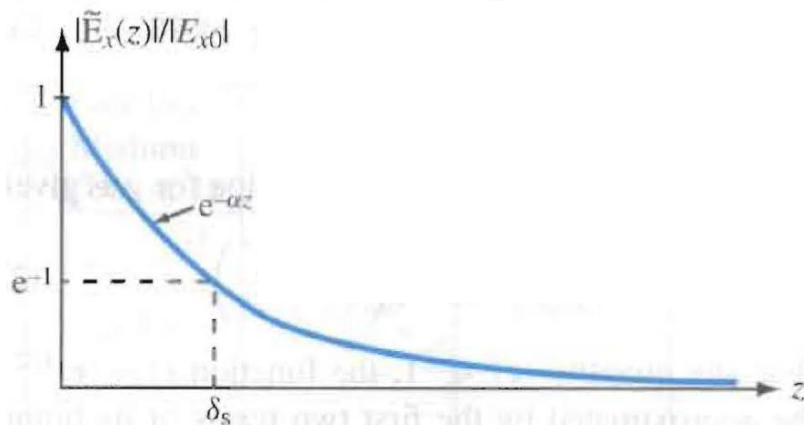
Figure 2.2. Electric field attenuation curve. [10]

Propagation is in the z direction and the attenuation constant α, in Np/m, is defined by

$$\alpha = \omega \left\{ \frac{\mu \varepsilon'}{2} \left[\sqrt{1 + \left(\frac{\varepsilon''}{\varepsilon'}\right)^2} - 1 \right] \right\}^{1/2} , \qquad (2.10)$$

where $\varepsilon' = \varepsilon$ and $\varepsilon'' = \sigma/\omega$. Note that these equations hold only for linear, isotropic, homogeneous media.

Equation (2.10) shows that signal attenuation depends not only upon a material's electromagnetic parameters but also the frequency of the signal itself. This explains the first great dilemma in GPR, frequency selection. Researchers ideally use extremely high frequency signals in the GHz range to achieve fine spatial resolution, however high frequency signals attenuate quickly when traveling through lossy media like soil or clay. Thus there is a practical limit to the penetration depth of high frequency, high resolution radar signals. The alternative option is to use lower frequency signals with greater penetration depth but larger resolution limits. As a

consequence, frequency range is constantly adjusted in GPR systems according to the depth of

the target and composition of the surrounding soil or ice.

Moisture content is often the most significant factor for determining a soil's dielectric

constant. Table 1 [1] shows conductivity and relative permittivity values for a wide variety of

natural materials. Moisture content causes the large variation in permittivity values seen on the

right; low permittivity ranges are due to dry conditions while the high ranges below them indicate

that the material is saturated with water. For this reason materials like clay or soil soaked after

heavy rain are harder to penetrate than their dry counterparts.

Table 1. Typical conductivity and permittivity values for common subsurface materials. [1]

Material	Static conductivity, σ_s (mS/m)	Relative permittivity, ε_{ave}
Air	0	1
Clay – dry	1–100	2–20
Clay – wet	100–1000	15–40
Concrete – dry	1–10	4–10
Concrete – wet	10–100	10–20
Freshwater	0.1–10	78 (25 °C)–88
Freshwater ice	1–0.000001	3
Seawater	4000	81–88
Seawater ice	10–100	4–8
Permafrost	0.1–10	2–8
Granite – dry	0.001–0.00001	5–8
Granite – fractured and wet	1–10	5–15
Limestone – dry	0.001–0.0000001	4–8
Limestone – wet	10–100	6–15
Sandstone – dry	0.001–0.0000001	4–7
Sandstone – wet	0.01–0.001	5–15
Shale – saturated	10–100	6–9
Sand – dry	0.0001–1	3–6
Sand – wet	0.1–10	10–30
Sand – coastal, dry	0.01–1	5–10
Soil – sandy, dry	0.1–100	4–6
Soil – sandy, wet	10–100	15–30
Soil – loamy, dry	0.1–1	4–6
Soil – loamy, wet	10–100	10–20
Soil – clayey, dry	0.1–100	4–6
Soil – clayey, wet	100–1000	10–15
Soil – average	5	16

2.3. Wave Reflection and Transmission

Radar exploits boundary reflections to make distance measurements. Whenever an electromagnetic wave impinges upon a boundary between two different materials, a portion of its energy continues forward while the rest is reflected away. A GPR receiver captures the reflected energy for post-processing. The electromagnetic parameters defined earlier and the signal's angle of incidence play a large role in both the amount of energy reflected as well as the direction of its reflection. Understanding boundary reflection is essential for realizing the limitations of an FLGPR system. Chapter 8 of [10] provides full derivations and figures for conclusions found below.

Incident plane wave

Transmitted plane wave

Reflected plane wave

Medium 1
η_1

Medium 2
η_2

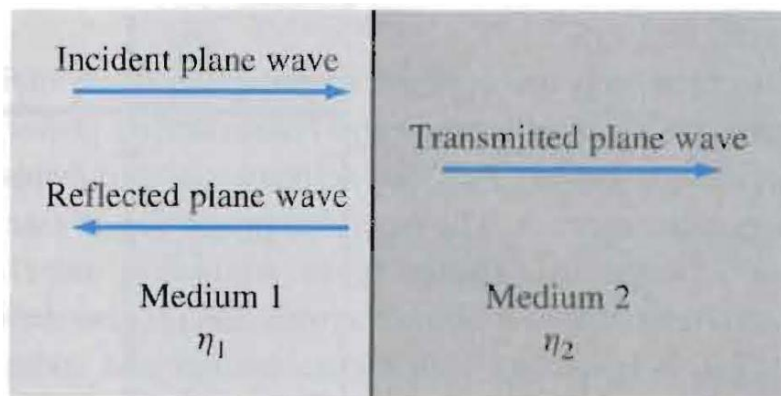**Figure 2.3. Normally incident, reflected and transmitted waves at a flat boundary. [10]**

The simplest case of wave reflection is a plane wave normally incident upon a boundary between two materials (Fig. 2.3). Assuming again that neither medium holds excess charge, the reflected and transmitted waves, respectively, are defined by

$$E_0^r = \left(\frac{\eta_2 - \eta_1}{\eta_2 + \eta_1}\right) E_0^i = \Gamma E_0^i, \tag{2.11}$$

$$E_0^t = \left(\frac{2\eta_2}{\eta_2 + \eta_1}\right) E_0^i = \tau E_0^i. \tag{2.12}$$

Here E_0^i, E_0^r and E_0^t are the incident, reflected and transmitted electric field magnitudes, respectively. The character η denotes intrinsic impedance. Intrinsic impedance for lossless and lossy media is defined by

$$\eta_{lossless} = \sqrt{\frac{\mu}{\varepsilon}}, \tag{2.13}$$

$$\eta_{lossy} = \sqrt{\frac{\mu}{\varepsilon'}}\left(1 - j\frac{\varepsilon''}{\varepsilon'}\right)^{1/2}. \tag{2.14}$$

Finally, Γ, known as reflection coefficient, is the ratio of reflected electric field magnitude to incident electric field magnitude. Reflection coefficient is utilized extensively in electromagnetic transmission and reflection analyses. For nonmagnetic media ($\mu = \mu_0$), reflection coefficient is

$$\Gamma = \frac{\sqrt{\varepsilon_{r1}} - \sqrt{\varepsilon_{r2}}}{\sqrt{\varepsilon_{r1}} + \sqrt{\varepsilon_{r2}}}. \tag{2.15}$$

The greater the disparity between the relative permittivity of two materials at a boundary, the more energy that will be reflected at the interface.

In the case of the basic GPR study here, a wave incident upon a boundary at an oblique rather than normal angle adds only the complexity of Snell's Law. Snell's Law describes the relationship between the angles of incidence θ_i, reflection θ_r and transmission θ_t. Equation (2.16) shows Snell's law of reflection.

$$\theta_i = \theta_r \tag{2.16}$$

(a) $n_1 < n_2$ (b) $n_1 > n_2$

(c) $n_1 > n_2$ and $\theta_i = \theta_c$
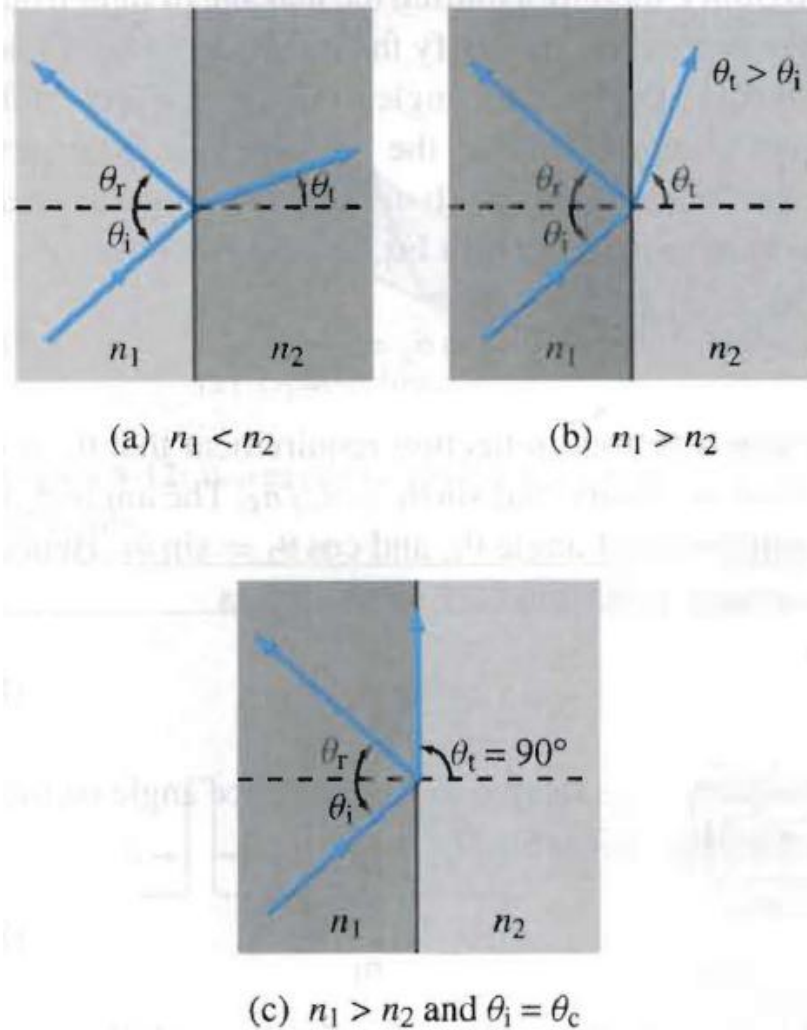
Figure 2.4. Plane wave experiencing (a) inward refraction, (b) outward refraction and (c) critical refraction. [10]

That is, the angle of the incident wave, measured with respect to the boundary normal, is equal to the angle of reflection, also measured against the boundary normal. Snell's law of refraction relates angles of incidence and transmission to one another, given nonmagnetic materials, in Equation (2.17).

$$\frac{\sin \theta_t}{\sin \theta_i} = \frac{\eta_2}{\eta_1} = \sqrt{\frac{\varepsilon_{r1}}{\varepsilon_{r2}}}$$

(2.17)

Snell's law of refraction shows that when a wave travels from high to low permittivity, the transmitted portion refracts inwardly towards the boundary normal on the high permittivity side. Conversely, a wave reflects outwardly away from the boundary normal if it travels from low to high permittivity. In this second case, when the transmitted wave angle $\theta_t = \pi/2$, that is, runs 90° from the boundary normal, no energy is transferred into the second medium (see Fig. 2.4 for examples of each case). Rather, the transmitted energy simply flows along the boundary surface, never penetrating the second material. This phenomenon is known as total internal reflection. The angle of incidence that corresponds to total internal reflection is the critical angle θ_c, defined by

$$\sin\theta_c = \sqrt{\frac{\varepsilon_{r2}}{\varepsilon_{r1}}}. \tag{2.18}$$

In an FLGPR system, the radar signal travels first through air and then enters the ground. There is an incidence angle known as the Brewster angle at which all incident energy of parallel polarization is transmitted through a boundary.

$$\theta_B = \tan^{-1}\sqrt{\frac{\varepsilon_{r2}}{\varepsilon_{r1}}} \tag{2.19}$$

A wave is parallel polarized if its electric field lies in the plane of incidence while its magnetic fields are perpendicular to the plane of incidence. The plane of incidence is the plane that contains the boundary normal and the propagation vector of the incoming radiation. Polarization is not a concern for the simulations performed in this paper.

At the same time, total internal reflection is an issue as FLGPR energy attempts to enter the ground. Because the waves travel from low permittivity air to high permittivity soil, a large portion of their energy reflects off the ground's surface and is lost into the distance. In effect, this energy is trapped in the atmosphere due to total internal reflection. Total internal reflection of incident radar energy is one of the reasons that FLGPR radar returns are so much weaker than their downward looking GPR counterparts.

The primary reason that FLGPR returns are weak is the relationship between θ_i and θ_r. Because the Brewster angle exists only at one finite point in the swath being scanned by an FLGPR system, most incident energy reflects off the ground's surface and propagates away into the distance. Only normal incidence electromagnetic waves reflect directly back at the receive antenna. Thus only a tiny amount of energy will find a path into the ground, reflect off the target, return to the receive antenna. The vast majority of energy broadcast from FLGPR systems never returns to its source.

2.4. Radar Frequency Content

Another important consideration for radar systems is frequency content. Many FLGPR systems transmit UWB signals, often of bandwidth 5 GHz or greater, in order to achieve high spatial resolution of a target. A variety of methods produce such large bandwidth signals including frequency stepping, frequency sweeping and high frequency voltage pulses. This UWB approach is generally known as a "time-domain" technique because it exploits travel time and phase shift between transmitted and received signals to gather range information.

Although a wide range of frequency content offers good spatial resolution, it is also particularly susceptible to clutter. Clutter, in the most general sense, is all energy received from reflections off of objects other than the target of interest. An obvious example of clutter is buried

litter. An old glass bottle causes wave reflections and registers at the receiving end of an FLGPR system, but because it is not the target of interest, it is considered clutter. In this way any buried trash, detritus and debris serve to clutter GPR readings. In war zones shrapnel and blast particles are a significant source of clutter.

There is more to clutter than just foreign objects, however. As discussed earlier, electromagnetic reflections occur anywhere dielectric constant changes; a shift in soil type causes unwanted reflections back to the receiver. Differences in local moisture content, uneven, cracked and rutted road surfaces and underground rock formations all introduce clutter into GPR measurements. Clutter is the largest impediment to the success of FLGPR.

As a result, because UWB signals are able to so well resolve the target of interest, they also are equally likely to resolve clutter as well. This results in messy, unreadable GPR signals in which distinguishing between target and clutter is nearly impossible. Thus even high resolution UWB radar signals exhibit significant weaknesses when searching for underground objects. Frequency choice and post-processing analysis in FLGPR systems are important topics that the results of this paper address.

2.5.   A Transmit Antenna

The final, significant component of an FLGPR system is the transmit antenna. The transmit antenna must be both directional and capable of radiating UWB signals. A directional antenna radiates energy in a certain direction rather than uniformly in every direction. Though only an isotropic radiator, a fictional antenna used for theoretical electromagnetic analysis, can truly radiate energy equally in every direction, some real antennas come quite close. A Hertzian dipole antenna, for example, radiates completely evenly in two dimensions (Fig. 2.5). Finding an appropriately directional antenna is imperative for the simulations ahead.
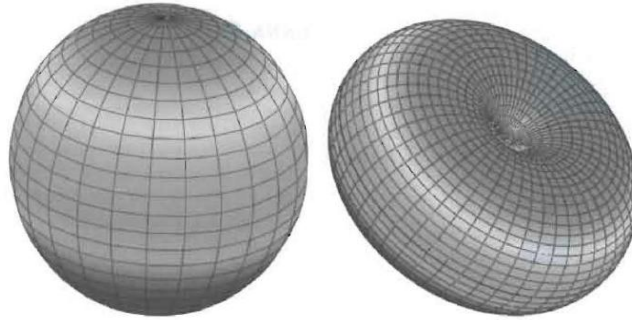
18

Figure 2.5. Radiation patterns for an isotropic radiator (left) and a Hertzian dipole (right). [1]

In addition to a certain directivity, FLGPR also requires high transmit bandwidth. Input impedance, reflection coefficient and ultimately voltage standing wave ratio (VSWR) determine an antenna's ability to transmit energy. The VSWR of an antenna at a certain frequency depends upon the transmission line impedance of the signal source and the input impedance of the antenna at that frequency. The reflection coefficient at the antenna is given by Equation (2.20). In this case the boundary is the connection between the signal source and the antenna and the reflected and transmitted quantities are voltage and current, rather than electric and magnetic fields.

$$\Gamma(\omega) = \frac{Z_{in}(\omega) - Z_g(\omega)}{Z_{in}(\omega) + Z_g(\omega)} \tag{2.20}$$

VSWR is a measure of how much energy reflects back into the signal source, where a VSWR of 1 indicates that no energy reflects back and a VSWR of infinity indicates that all energy reflects back. VSWR is calculated by

$$VSWR(\omega) = \frac{1 + |\Gamma(\omega)|}{1 - |\Gamma(\omega)|}. \tag{2.21}$$

In order for an antenna to transmit a signal of certain bandwidth, its VSWR must be acceptably low at every frequency within that bandwidth (Fig. 2.6) [11]. The antenna design community generally accepts a VSWR of 2 or less as a good match between a load and a source. High bandwidth antenna design is a difficult task filled with a great deal of trial and error.
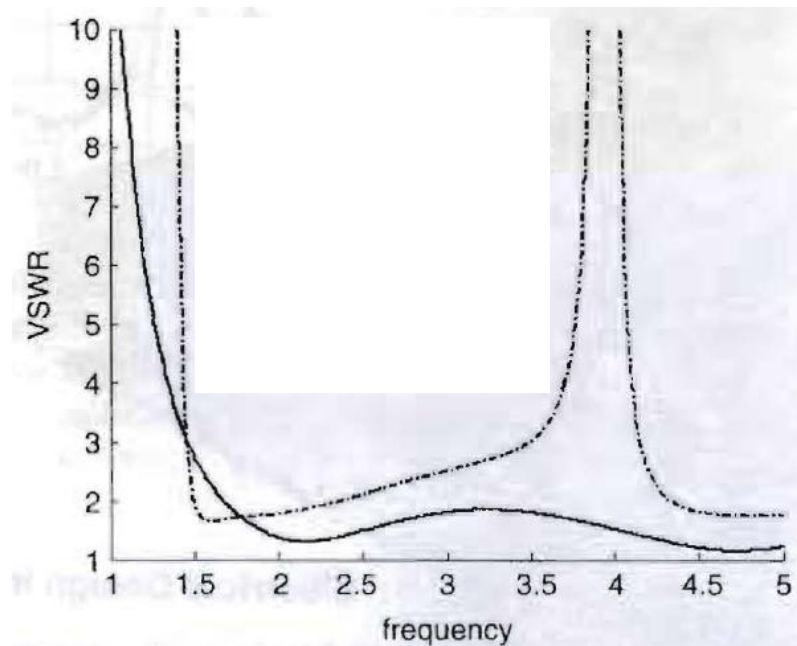
Figure 2.6. An example of VSWR vs. frequency for two Vivaldi antenna array configurations. [11]

With solid understanding of the basic theory behind FLGPR's most debilitating limitations, accurate and meaningful simulations can be designed to test the ability to detect IEDs buried in wartime environments. However, accuracy of simulation results depends not only upon adhering to electromagnetic theory, but also upon awareness of the simulation method and its limitations.

Chapter 3: Finite Difference Time Domain Numerical Method

The finite difference time domain (FDTD) method is an electromagnetics analysis tool used for predicting and modeling real world radiation problems. Proper application of FDTD can yield understanding of topics as diverse as antenna design, MRI effects on the human body, upper atmosphere radiation in passenger planes, signal behavior in microwave circuits and even ground penetrating radar. FDTD is used in this paper to explore signal to clutter ratio for a simple FLGPR setup. Unless otherwise specified, all of the following derivations can be found in [12].

3.1. FDTD Basics

The FDTD method for electromagnetics is built upon numerical solutions to Maxwell's equations, which can be expressed in both the time domain and frequency domain. For example,

$$\nabla \times \boldsymbol{E} = -\mu \frac{\partial \boldsymbol{H}}{\partial \mathrm{t}} \Leftrightarrow \nabla \times \widetilde{\boldsymbol{E}} = -j\omega\mu\widetilde{\boldsymbol{H}}. \tag{3.1}$$

The time domain solutions have two main advantages over those in the frequency domain. With use of the fast fourier transform (FFT) algorithm, time domain data gives results at all frequencies simultaneously, while frequency domain solutions compute results one frequency at a time. In addition, for frequency domain solutions the only possible method of excitation, or introducing electromagnetic energy into the simulation space, is a sine wave. In the time domain any time-varying excitation signal, and thus its corresponding frequency content, can be created. Taking finite differences of Maxwell's time domain equations is the best choice for developing an FDTD algorithm.

A finite difference is an approximation of a derivative. Forward, backward and centered differences are the three main methods of approximating a derivative. To approximate the derivative of an electric field function at a point in time, t, one must add a small increment, Δt, to that point in time and measure the change in the output of the function. Forward differences add Δt to that point and are most accurate at $t + \frac{\Delta t}{2}$ while backward differences subtract Δt from that point and are most accurate at $t - \frac{\Delta t}{2}$. Centered differences, shown below, are most accurate exactly at t and are best suited for use in FDTD.

$$\frac{d\boldsymbol{E}}{dt} \approx \frac{\boldsymbol{E}\left(t + \frac{\Delta t}{2}\right) - \boldsymbol{E}\left(t - \frac{\Delta t}{2}\right)}{\Delta t} \tag{3.2}$$

3.2. Update Equations in One Dimension

The simplest formulation of FDTD solves two of Maxwell's Equations assuming that the medium of interest is lossless and that ε and μ are constants.

$$\nabla \times \boldsymbol{E} = -\mu \frac{\partial \boldsymbol{H}}{\partial t} \tag{3.3}$$

$$\nabla \times \boldsymbol{H} = \varepsilon \frac{\partial \boldsymbol{E}}{\partial t} \tag{3.4}$$

Further assuming that the energy is propagating in the z direction as a plane wave and that only E_x and H_y are nonzero field components, Equation (3.3) can be approximated using centered differences for both the spatial and temporal derivatives,

$$\frac{E_x^{n\Delta t}[(k+1)\Delta z] - E_x^{n\Delta t}(k\Delta z)}{\Delta z} = \mu \frac{H_y^{(n+1/2)\Delta t}[(k+1/2)\Delta z] - H_y^{(n-1/2)\Delta t}[(k+1/2)\Delta z]}{\Delta t}. \qquad (3.5)$$

A similar approximation to Equation (3.4) exists in [12]. In the FDTD equations above and below, rather than serving as exponents, the superscripts represent current step in time, where $t = n\Delta t$. Similarly, k denotes current spatial step, where $z = k\Delta z$. Finally, complete solutions for electric and magnetic field values at a particular location z and time t are,

$$H_y^{n+\frac{1}{2}}\left(k + \frac{1}{2}\right) = H_y^{n-\frac{1}{2}}\left(k + \frac{1}{2}\right) - \frac{\Delta t}{\mu \Delta z}[E_x^n(k+1) - E_x^n(k)], \qquad (3.6)$$

$$E_x^{n+1}(k) = E_x^n(k) - \frac{\Delta t}{\varepsilon \Delta z}\left[H_y^{n+\frac{1}{2}}\left(k + \frac{1}{2}\right) - H_y^{n+\frac{1}{2}}\left(k - \frac{1}{2}\right)\right]. \qquad (3.7)$$

With clever use of the centered differences approximation technique, Yee [13] engineered the FDTD update equations such that E-fields are calculated $\frac{\Delta t}{2}$ and $\frac{\Delta z}{2}$ away from H-fields. Though E and H-fields technically exist at the same point in space, this approximation allows for a simple calculation technique that requires basic algebra operations instead of solutions to systems of simultaneous equations. The Yee cell (Fig. 3.1) visually represents this concept in three dimensions. The spatial separation between the field values is created by placing E-field values on the edges of the cube and H-field values on the cube's faces. The lengths of the cube's sides are the spatial step sizes $\Delta x, \Delta y$ and Δz.
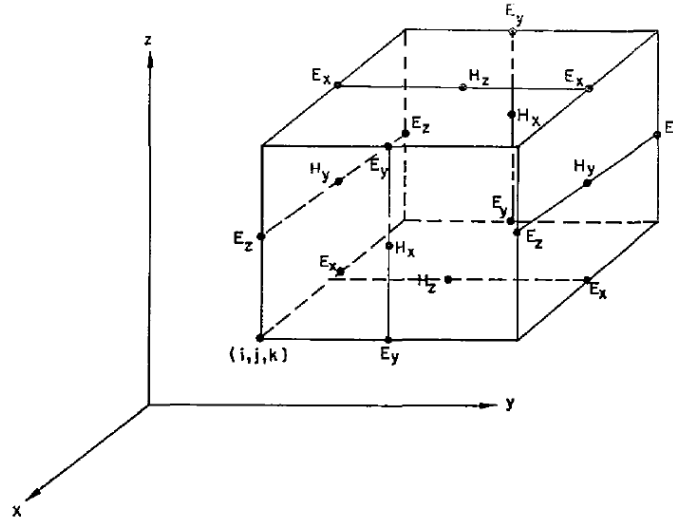
Figure 3.1. Yee cell with electric fields on edges and magnetic fields on faces. [13]

Given the offset nature of field calculations in FDTD, the computation algorithm is simple. Initial conditions must be set first, so at time $t = 0$ all E-fields are set to zero throughout the space and, because of the $\frac{\Delta t}{2}$ spacing between field calculations, at $t = 0.5\Delta t$ all H-fields are set to zero. At $t = \Delta t$, using Equation (3.6), the E-fields at every point are calculated using the old E-field values at each point and the current H-field values at the sides of every E-field point. Next, at $t = 1.5\Delta t$, using Equation (3.5), the H-fields at every point are calculated using the old H-field values at each point and the current E-field values at the sides of every H-field point. Time progresses to $t = 2\Delta t$ and the E-fields are calculated once more, followed by the H-fields, and so on; this is generally known as the "leap frog" method.

A disconnect exists between theory and implementation of FDTD, however. When performed on a computer, E and H-field values are calculated and stored at one point without the spatial the shift between them. Also, both field values are calculated during the same time step, without the half step shift between them. This discrepancy exists because FDTD is an approximation. Adding the temporal and spatial shifts between the E and H-field calculations is a theoretical falsehood that allows Maxwell's Equations to simplify to Equations (3.5) and (3.6).

These equations require only simple arithmetic to solve which makes them quick and easy for a computer to calculate. The electromagnetics community is fortunate that papers subsequent to [13] proved the approximation sufficiently accurate for modeling propagation of electromagnetic waves.

3.3.   Absorbing Boundary Conditions

FDTD is used to model wave propagation in bounded simulation environments. However, as implied by Equations (3.6) and (3.7) calculation of each field component requires knowing the values of field components adjacent to the location in question. A problem arises at the boundaries of the simulation space where the final field component has no adjacent value outside the space. As a result, special boundary conditions must be formulated to deal with the edges of a simulation space.

There are four main methods of dealing with FDTD boundary conditions. The first and most primitive is setting all exterior *E*-field values to zero. This is equivalent to surrounding the entire simulation space with a perfect electric conductor (PEC). PEC is only desirable in rare situations, however, because it completely reflects all energy incident upon its surface.

The second method is known as the surface equivalence theorem approach. In this technique, the nonexistent outer fields needed to calculate values at the edge of the simulation space are determined using the surface equivalence theorem. The surface equivalence approach is unpopular due to its computational intensity and likelihood of round-off error.

Another solution to the boundary problem is the Mur boundary condition. The first order Mur boundary condition is effective in one dimensional simulations because it satisfies the assumptions that the incoming wave is planar and that it is incident perpendicular to the boundary. It looks back one time step and in one spatial step to estimate the new field value at the

boundary. Second and third order Mur boundary conditions that look back two and three steps can be used in two or three dimensional simulations; their results, however, are unreliable because in multiple dimensions wave fronts can no longer be assumed to be planar and thus the Mur solution is inaccurate.

The most effective and popular solution to the FDTD boundary problem is a perfectly matched layer (PML). First described in 1994 by Berenger [14], PML surrounds the simulation space with a layer of absorbing material designed to fully attenuate all wave energy that enters its domain. The absorbing material formulated in a PML boundary is not physically realizable; rather it is a numerical technique that dampens incoming signals without reflecting any energy back into the simulation space. The real world analog of PML is an anisotropic medium, where the electrical properties of the material depend upon the vector direction of the incident fields.

PML typically includes many layers of absorbing material, whose conductivity increases with depth into the absorber. Typically, anywhere between eight and 16 PML layers are used, whose conductivity profile varies following a parabolic curve. That is, the first layer has a conductivity equal to that found at the simulation space edge, the second layer's conductivity is slightly larger, the third's is even larger, and so on according to a parabolic function. The final layer of the PML is PEC. This ensures that any energy not completely attenuated after initially traveling through the PML bounces back and passes through it a second time. This technique runs the risk of bouncing small amounts of un-attenuated energy back into the simulation space, but PML has been designed and tested to ensure that such energy is negligible.

In a large three dimensional simulation, up to 16 additional layers of material, with 12 update equations per cell, adds significant size and time requirements. PML does not impose any limiting assumptions, however, and is so effective that the extra computational time is a

reasonable trade-off in modern simulations. PML is the boundary condition of choice for the simulations ahead.

3.4. Practical Issues

Certain practical conditions must be satisfied in order to achieve accurate results in an FDTD simulation. The first issue is cell size, or determination of the spatial step length. Though the Nyquist theorem suggests that only two step sizes per wavelength λ are necessary, most simulations set an upper limit to the step size defined by

$$minimum\ cell\ size = \frac{\lambda_{min}}{10}.$$
(3.8)

Here λ_{min} is the shortest wavelength found in the simulation.

Cell size is usually a tenth of the shortest wavelength or smaller because of error induced by approximations made in the formulation of the FDTD method. One such approximation, known as "stair casing", results from modeling curved surfaces with discrete cubes. Another, grid dispersion, is a consequence of discretizing time and space in Maxwell's Equations. Research has shown, however, that these errors can be mitigated if a sufficiently small cell size is chosen, often down to a twentieth or fortieth of the smallest wavelength present.

Time step size depends upon cell size. Because FDTD calculations rely on local field values, the time step can be no longer than the time required for the wave to travel from, for example, an E-field location to its adjacent H-field component. In the original one dimensional example, if the maximum possible distance a wave can travel in half a time step is $\frac{v_{max}\Delta t}{2}$, then

that distance can be no larger than the distance between two adjacent field values, $\frac{\Delta z}{2}$. The

Courant limit [12] defines maximum time step size as

$$\Delta t \leq \frac{\Delta z}{v_{max}}. \tag{3.9}$$

More complicated geometry analysis for the three dimensional case results in a Courant limit of

$$\Delta t \leq \frac{1}{v_{max}\sqrt{\frac{1}{\Delta x^2} + \frac{1}{\Delta y^2} + \frac{1}{\Delta z^2}}}. \tag{3.10}$$

Most simulations have some free space present, so v_{max} is typically the speed of light in free space, c. It can be shown that a time step smaller than the Courant limit is also liable to introduce error into FDTD calculations. Only in uncommon situations is such a small time step necessary.

Once appropriate values for cell size and time step are determined, the simulation can be modeled and performed on a computer.

3.5.   Computational Requirements

FDTD simulations are computationally intensive and can require significant computer resources. Each E and H-field component is stored as a 4 byte floating point number, with six field components per cell. In addition, each cell holds six material identification numbers, indicating what medium that cell represents, stored as 1 byte integers. Because initial instructions and overhead are generally negligible, memory required for a simulation is determined by

$$\text{storage(bytes)} = 30N, \tag{3.11}$$

where N is the total number of cells in the simulation space.

Execution time is another important factor when running simulations. A conservative estimate for calculations required in a simulation is 15 floating point operations per field component per time step. In the three dimensional case, where every cell contains six field components,

$$\text{no. of calculations per time step} = 90N \frac{f.p.ops.}{time\ step} \tag{3.12}$$

In a cubical simulation space, the number of time steps required to allow all transients to die out is approximately $10\sqrt{3}N^{\frac{1}{3}}$. Thus, a conservative estimate for the number of calculations necessary in a cubical simulation space is

$$\text{no. of calculations} = 1600N^{\frac{4}{3}} f.p.ops. \tag{3.13}$$

As simulations increase in size and complexity, their computational requirements quickly burgeon as well. It is not uncommon for FDTD simulations to run for hours or even days on standard household computing machines. Many vendors offer enhanced processors designed for computationally intensive simulations; however, they are usually prohibitively expensive for the casual user. Intelligent and efficient simulation design is essential for running feasible, accurate FDTD experiments.

3.6. Final Notes

The FDTD update equations employed in professional simulation packages are much more complex than Equations (3.5) and (3.6). Both conductivity and magnetic conductivity, a quantity that simulates magnetic loss, are incorporated into Maxwell's equations before taking centered differences. Also, in order to model different materials in a simulation space, every electrical parameter must be a function of position. Beyond that, materials whose electrical properties are frequency dependent require entirely different formulation methods and result in new and more complicated update equations. Although discussion of these topics is beyond the scope of this paper, it is worth acknowledging the complexity of FDTD for electromagnetics. It has taken over 40 years of testing and research to create the accurate, easy-to-use tool that FDTD is today.

Chapter 4: Simulation Design

XFdtd 7 provides the FDTD simulation workspace for the simulations ahead. The newest edition of professional electromagnetics simulation software by Remcom, XFdtd 7 is built for dynamic and complicated industry applications. It is intuitive, easy to use and employs a variety of safeguards to avoid inaccurate results. Despite XFdtd 7's simplicity and professional quality, however, the user ultimately must determine most simulation constraints. Location, soil type, weather, IED type, antenna design and various FDTD parameters including cell size and time step all must be selected in order to achieve valid simulation results.

4.1. Location and Material Parameters

The wars and subsequent insurgencies in Iraq and Afghanistan originally inspired research into IED detection with FLGPR. Because the conflict in Afghanistan recently experienced a troop surge, while the Iraq war is slated to close by the end of 2011, Afghanistan is chosen as the country of interest for the simulations. A targeted search through the Global Terrorism Database, built by the University of Maryland, reveals that Kabul, Afghanistan's capitol, experienced the largest number of attacks between 2001 and 2008 (Fig. 4.1) [14]. Kabul's soil and climate types are used to define the parameters implemented in the FDTD simulations.
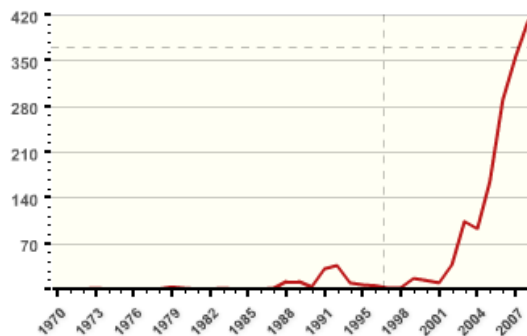
Figure 4.1. Terrorist attacks per year in Afghanistan; the majority occurred in Kabul. [14]

A soil map of Afghanistan (Fig.4.2) [16], shows that the regional soil type in Kabul is rocky land with lithic haplocambids. According to [17], Aghanistan's climate resembles that of a semiarid steppe, with dry hot summers and cold winters. Assuming the FLGPR measurements are not taken directly after a rainstorm, land in Kabul generally corresponds to dry, sandy soil, found in Table 1 (pg. 9). The approximate median of the extremes given in Table 1 are used, so dry, sandy soil is modeled with $\varepsilon_r = 5$ and $\sigma = 0.05$ mS/m. For the simulation that explores the impact of heavy rain on FLGPR measurements, wet, sandy soil values are taken from Table 1 (pg. 11). Muddy earth after a rainstorm is approximated with $\varepsilon_r = 20$ and $\sigma = 50$ mS/m.
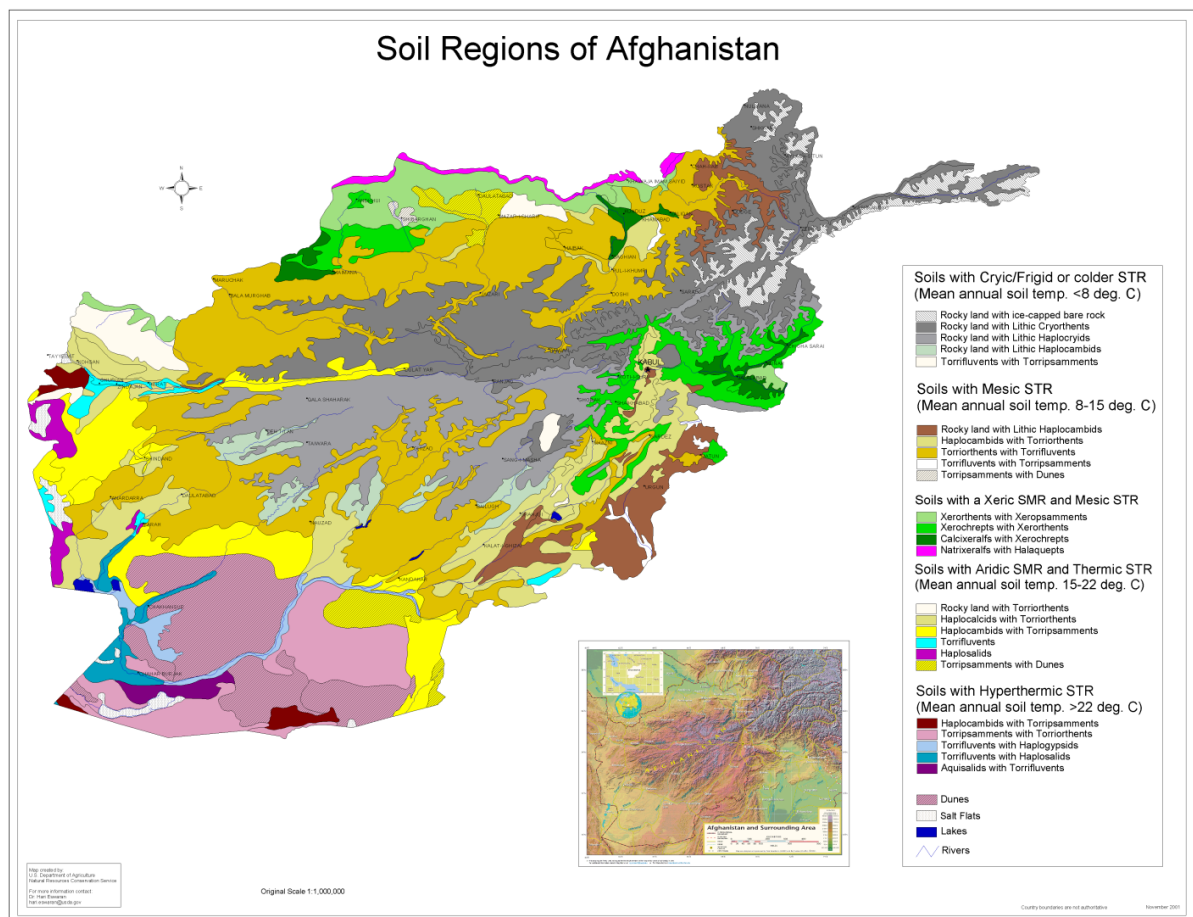
Figure 4.2. Soil regions in Afghanistan. [16]

Gravel roads across the countryside are assumed to be composed of chunks of granite, sandstone and limestone. Due to time constraints, a gravel road in XFdtd is composed of 42 mm by 26 mm rectangles that follow a predictable distribution pattern. Dielectric constant and height vary between each gravel type; granite chunks are 30mm tall with $\varepsilon_r = 8$ and $\sigma = 0.01$ mS/m, limestone chunks are 20 mm tall with $\varepsilon_r = 6$ and $\sigma = 0.001$ mS/m and sandstone chunks are 25 mm tall with $\varepsilon_r = 5.5$ and $\sigma = 0.001$ mS/m (Fig. 4.3). Though not a physically accurate depiction of gravel, the design is a reasonable approximation of an irregular gravel surface.
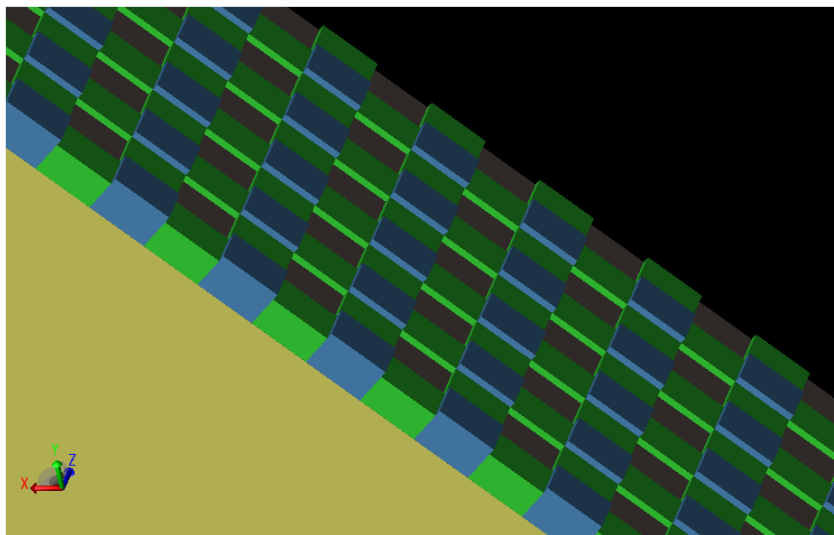
Figure 4.3. Gravel road modeled in XFdtd 7.

Plastic and metal clutter, simulating shrapnel and buried litter, are given arbitrary shapes and sizes smaller than the target IED. Plastic is modeled with $\varepsilon_r = 2.5$ [6] and $\sigma = 0$ while metal shrapnel is modeled with $\varepsilon_r = 1$ and $\sigma = 1 \times 10^7$ S/m. These types of clutter are buried next to and above the mine.

4.2. Target IED

In order to achieve results comparable to those found in [5], military grade anti-tank mines are chosen as the IED target of interest. The only details given of the anti-tank mine are its

diameter, approximately 250 mm, its burial depth, between 50 and 100 mm, and its plastic composite material. Given those initial clues, the VS-3.6 is chosen for simulation. The VS-3.6 is an Italian, plastic anti-tank mine known to be used by combatants as a form of IED. Figure 4.4 shows an image and internal diagram of a VS-2.2, the smallest model in the VS family of plastic mines; with the exception of size, the VS-3.6 and VS-2.2 are approximately identical. In XFdtd 7, a cylinder with a diameter of 248 mm and a height of 100 mm comprises the lower body of the mine and another cylinder with a diameter of 90 mm and a height of 15 mm represents the pressure plate triggering mechanism on top (Fig. 4.5).
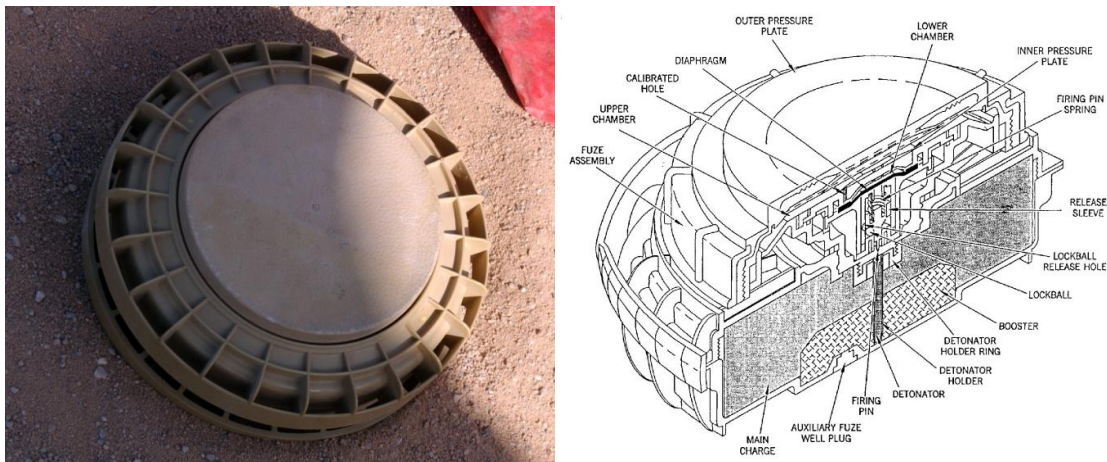
Figure 4.4. Photograph and internal diagram of the VS-2.2, smallest in the

VS mine family. [18]

Despite the complex inner workings of a high grade anti-tank mine like the VS-3.6, [6] shows that a landmine can be modeled as a solid cylinder with air pockets scattered inside. Because the dielectric constant of a mine's explosive compound is often quite close to that of its

plastic case, both cylinders are given $\varepsilon_r = 2.5$ and $\sigma = 0$ S/m. Time constraints and modeling

difficulties prevent the addition of air pockets to the mine in simulation.
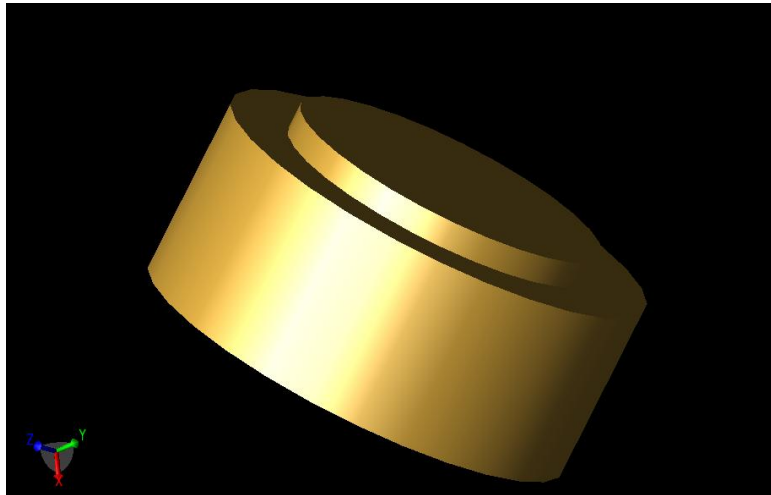

Figure 4.5. VS-3.6 plastic anti-tank mine modeled in XFdtd 7.

4.3.   Vivaldi Antenna

A Vivaldi antenna, also known as a tapered slot antenna, provides the high bandwidth

and directivity required in FLGPR simulation. The bandwidth of interest is $0.5 - 3$ GHz. This

bandwidth is chosen to achieve results comparable to those found in [5]. Vivaldi antenna design

involves a significant amount of trial and error, following only a few general guidelines.

Of the parameters shown in Fig. 4.6, rate of exponential growth, R_a, and cavity size, D_{sl},

strongly impact a Vivaldi antenna's performance. Large R_a and D_{sl} values increase antenna

radiation resistance at low frequencies, but can also cause unwanted fluctuations in resistance and

reactance throughout the frequency band of operation. Another guideline suggests that if the

antenna is built upon a circuit board, the substrate thickness should be approximately 0.1 times

the width of the overall antenna, where width is measured in the direction of H_a in Figure 4.6.

Finally, longer antennas, in general, have greater bandwidths and operate well at low frequencies.

References [19] and [20] investigate Vivaldi parameter design in greater detail, not necessary for purposes here.

Remcom provides a basic template for the Vivaldi antenna. Although the template's details are unknown, rigorous testing results in a useable antenna with reasonable VSWR throughout the 0.5-3 GHz bandwidth (Fig. 4.7). It is built with ground plates on the top and bottom of a dielectric insulating layer. The dielectric is, upon recommendation from Remcom, Duroid, with $\varepsilon_r = 2.32$ and $\sigma = 0$. The signal plate is sandwiched in the middle of the Duroid, hidden from view. The complete Vivaldi antenna is 360.5 mm wide, 360.5 mm long and 20 mm thick (Fig. 4.8). The ground and signal plates are PECs.

Vivaldi antennas are highly directive and exhibit a theoretical beamwidth of approximately 40 to 50 degrees. The calculated directivity results from simulation (Fig. 4.9) of the designed antenna reasonably agree well with theoretical expectations.
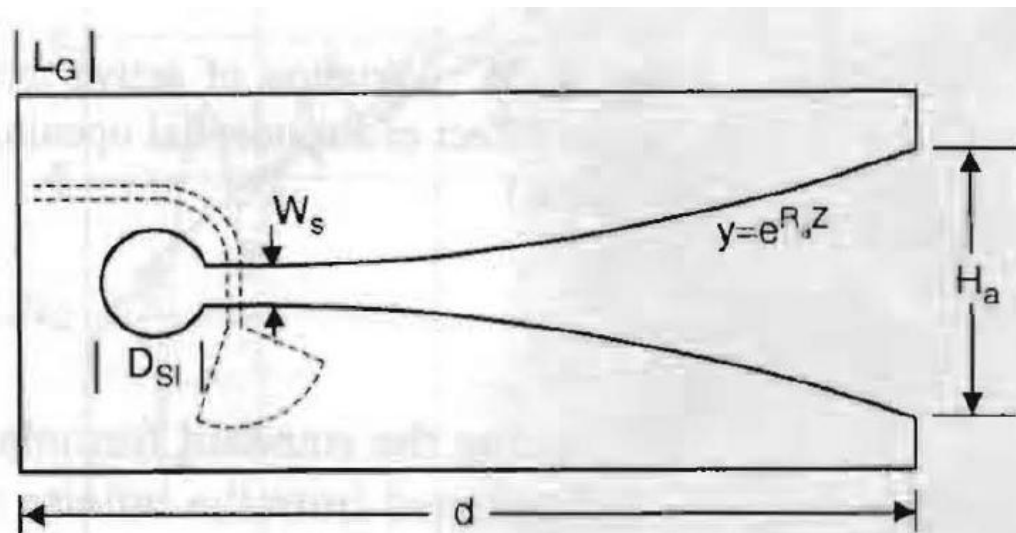
Figure 4.6. Parameters that define Vivaldi antenna behavior. [11]
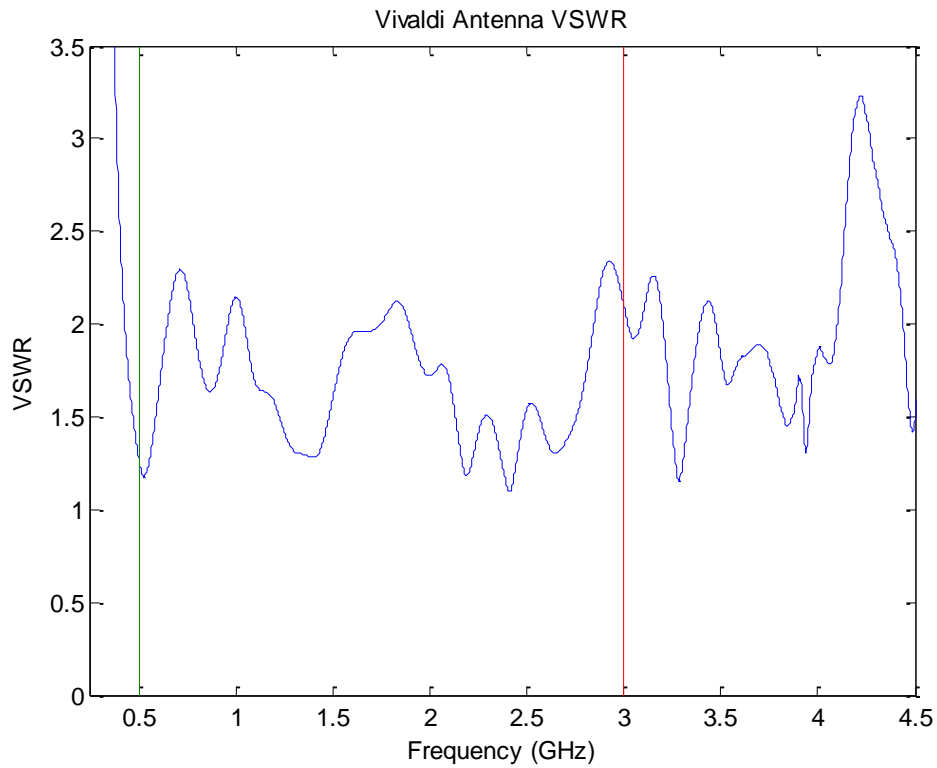
Figure 4.7. VSWR at the interface between the 50Ω signal source and the Vivaldi antenna; green and red lines mark the 0.5 – 3 GHz bandwidth.

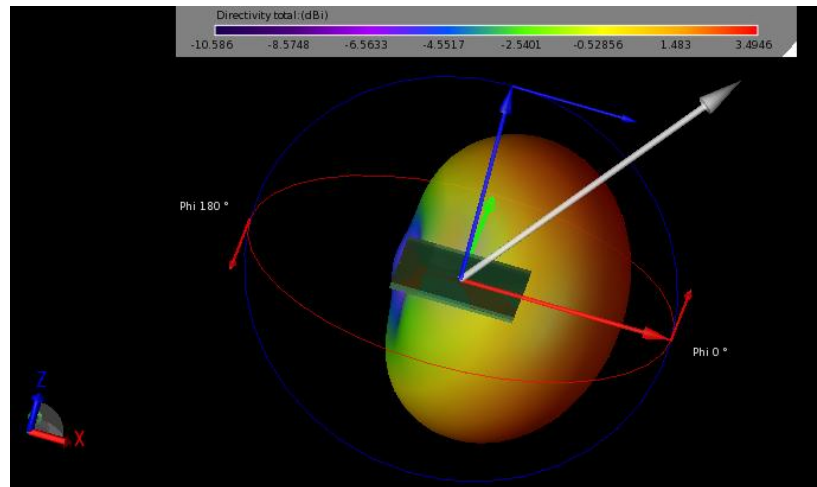Figure 4.8. Vivaldi antenna modeled in XFdtd 7; opacity is 50%, so the middle conductor curving down is visible.

Figure 4.9. Simulated directivity of Vivaldi antenna in XFdtd 7.

4.4.   Cell Size, Excitation Waveform and Boundary Condition

XFdtd 7's default behavior automatically chooses the time step length based upon the manually entered cell size. Because each simulation has different materials, including soil, gravel and shrapnel, the upper limit on cell size differs for every run. In order to compare results during post processing, however, it is helpful if every simulation has the same time step. To ensure that every simulation uses the same time step, the smallest cell size necessary, 2 mm, is manually applied to each simulation; the corresponding time step is 3.15867×10^{-12} seconds. Using what is, in some cases, an unnecessarily small cell size vastly increases memory and calculation time required for each simulation. This disadvantage is, however, offset by the increased accuracy and simplification of the post-processing tasks enabled by consistent time step length between simulations.

A Gaussian derivative waveform is used to excite the Vivaldi antenna. The Gaussian derivative possesses little low frequency and zero DC energy content, and is adequate for

simulating IED detection with FLGPR. A pulse width of 760 ps provides ample signal energy

between 0.5 and 3 GHz (Fig. 4.10).

Finally, a PML is used as the simulation boundary condition. Remcom suggests that only

seven PML layers are necessary to achieve accurate results. Testing shows that the PML

boundary is effective, and energy leaving the simulation space does not return. The boundary is

oriented such that it hugs the modeled soil's edges, with no intermediate free space between soil

and the PML boundary. This eliminates reflections from the transition between ground and free

space before the energy exits the simulation space.
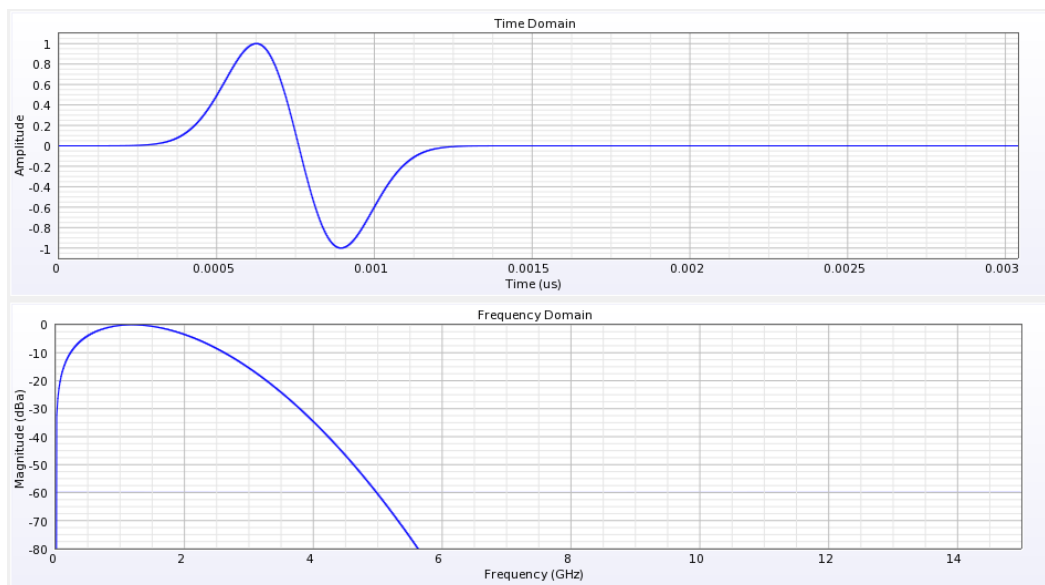
Figure 4.10. Gaussian derivative of width 760ps used as simulation excitation. Top: time-domain waveform. Bottom: waveform frequency content.

4.5. Post-Processing

Signal to clutter ratio cannot be directly calculated from XFdtd 7 simulation data.

Because the Vivaldi antenna does not have a VSWR of 1 throughout the simulation bandwidth, it

experiences significant ringing after the initial derivative Gaussian excitation. When waves

reflected from both mine and clutter finally return to the antenna, they mix with its ringing energy. Electric fields superpose, so the return energy is masked by the ringing. The performance of an antenna is dependent upon coupling with its surroundings. Thus there is no way to isolate its behavior from its environment, i.e. the target and clutter. Since there exists no baseline antenna behavior to subtract from each data set, the masking caused by the ringing cannot be avoided given this simulation configuration.

If, however, the antenna is located far enough away from the target that ringing dies out before the return energy arrives, signal to clutter ratio can be calculated. In this case, because the ringing is gone, the return signal is clearly visible and remains unmasked by the antenna behavior. Such a vast distance, however, requires an extremely large and lengthy simulation. Simulations of that scale are not feasible for a modest computer like the one used for the experiments here.

Despite the inability to directly calculate signal to clutter ratio, it remains possible to identify changes in simulation frequency content due to the presence of a mine. This requires two data sets per environment. The first data set results from simulating FLGPR in a given environment without a mine. The second data set is of the same environment with a mine present. Fast fourier transforms of both data sets are evaluated and the frequency response with the mine present is divided by the frequency response without the mine. This process generates the difference ratio caused by the presence of a mine:

$$\text{Mine Effect Response} = \frac{\text{FFT(data with mine present)}}{\text{FFT(data without mine present)}} \qquad (4.1)$$

Unfortunately, because plastic anti-tank mines reflect little electromagnetic energy, the differences between the simulation data with and without a mine are small. Proper data and graph

formatting, however, makes the impact of an IED's presence clear. All post-processing data

manipulation and graphical presentation are performed in MATLAB.

Chapter 5: Results

Four separate environments are tested, with two simulations run per environment. The first run of an environment simulates FLGPR readings without a VS-3.6 anti-tank mine present. The second run adds a target and simulates once more; other than the addition of the VS-3.6, no changes are made to the environment. The mine and antenna location and orientation are maintained constant throughout all tests of every environment. The four environments tested are free space, a smooth road with homogeneous soil, a gravel road and a muddy, rutted road with buried shrapnel. In order to maintain good Vivaldi performance, the antenna is aligned with the grid and avoid stair casing error. As a result the ground and mine are tilted 45 degrees to simulate the forward looking nature of FLGPR.

The FDTD simulation parameters are the same for all cases subsequently presented. The time step is 3.85167×10^{-12} seconds and $\Delta x, \Delta y$ and Δz are all 2 mm. The simulation space is a $950 \times 480 \times 260$ mm box with $475 \times 240 \times 130$ cells. On a student laptop with an Intel Pentium SU4100 processor and 3 GB DDR3 RAM, each simulation requires approximately 5 hours to complete. Completion is determined by a convergence check in XFdtd 7 set to -40 dB.

5.1. Free Space

See Figure 5.1 for an image of the environment model and Figure 5.2 for a planar slice of the simulation space, showing electric field propagation. Both images are captured directly from XFdtd 7's graphical user interface (GUI). Figures 5.3 and 5.4 show the time domain voltage signals at the antenna feed for each run. The derivative Gaussian excitation in the beginning is

clearly visible, as is the antenna ringing that follows. Because the energy returned from the plastic mine is weak, there is no obvious difference between the two waveforms.

Figures 5.5 and 5.6 show FFTs of each data set. Again, visual determination of differences between signal frequency content is impossible. Finally, Figure 5.7 shows mine effect ratio, defined earlier in Equation (4.1), from the two runs in free space.
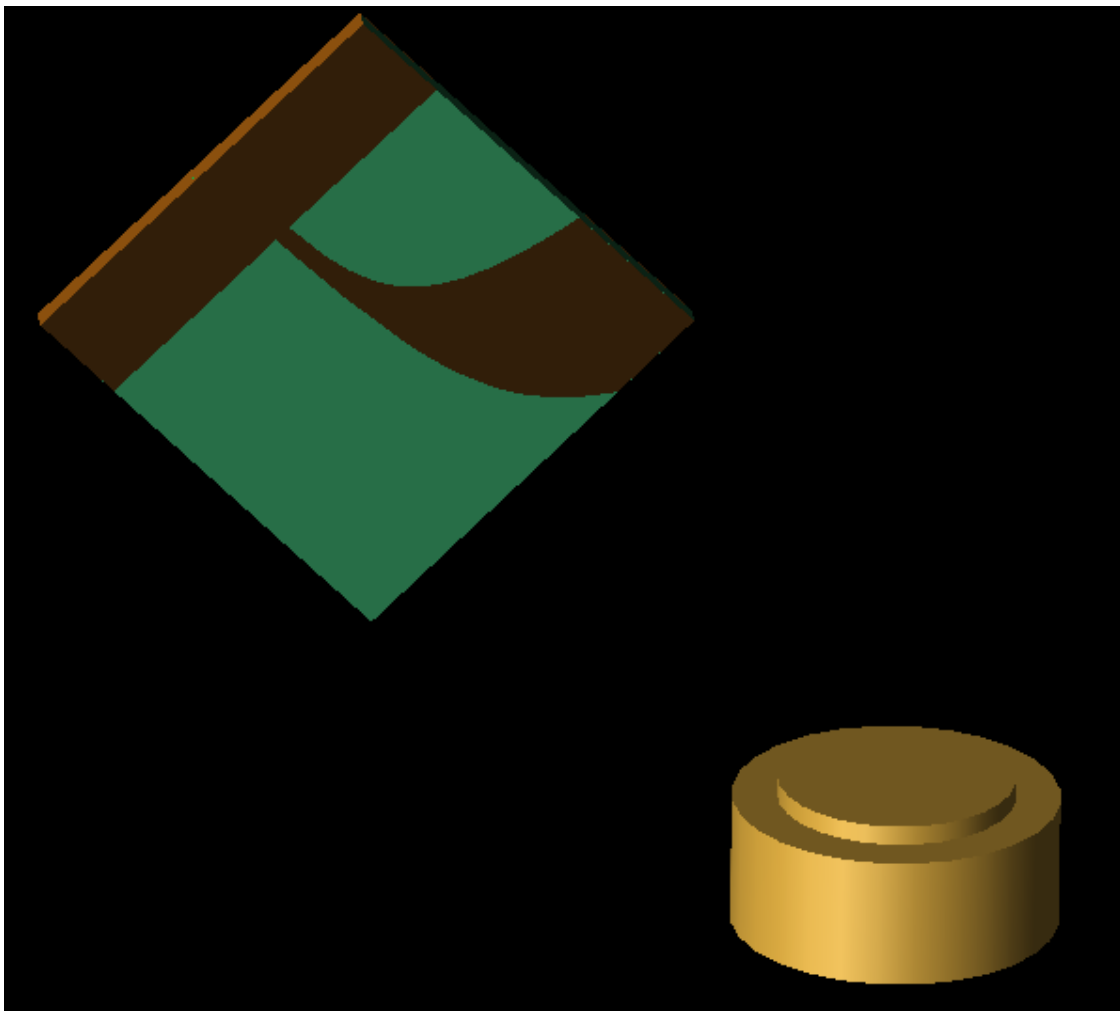

Figure 5.1. Screen capture of the XFdtd 7 GUI for the second run in free space.
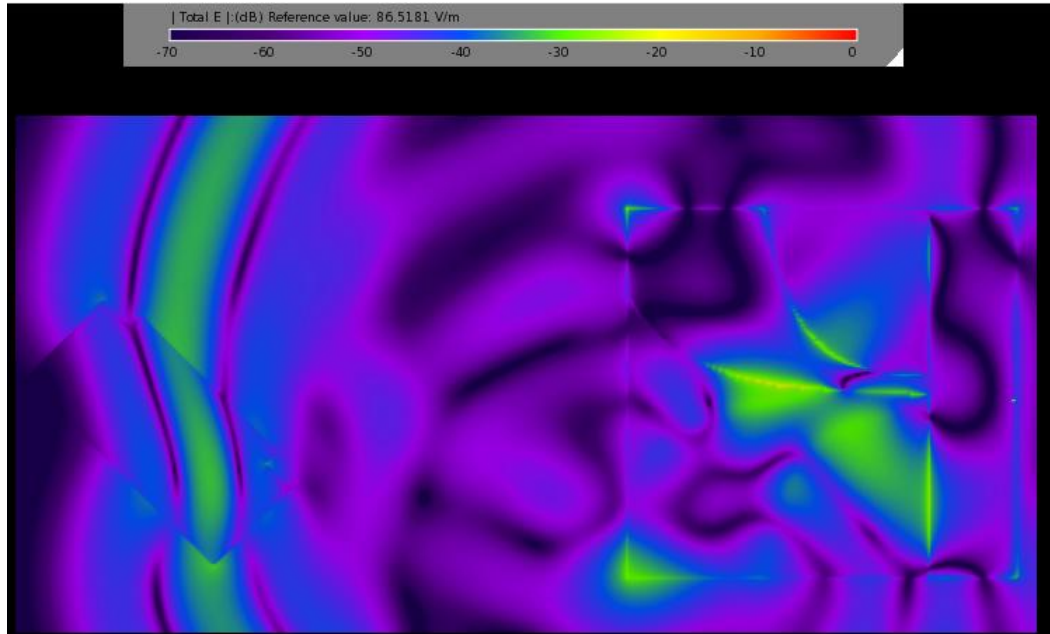
Figure 5.2. Screen capture of electric field propagation in 2-D, taken at time step 102; the antenna is on the right while the mine is visible on the left.
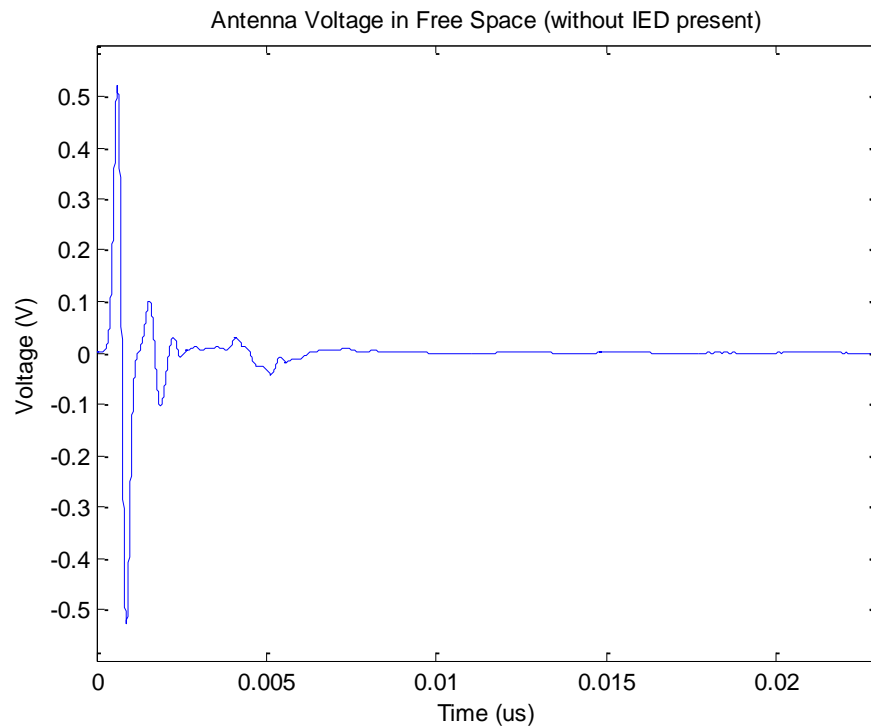
Figure 5.3. Antenna voltage in free space without an IED present.
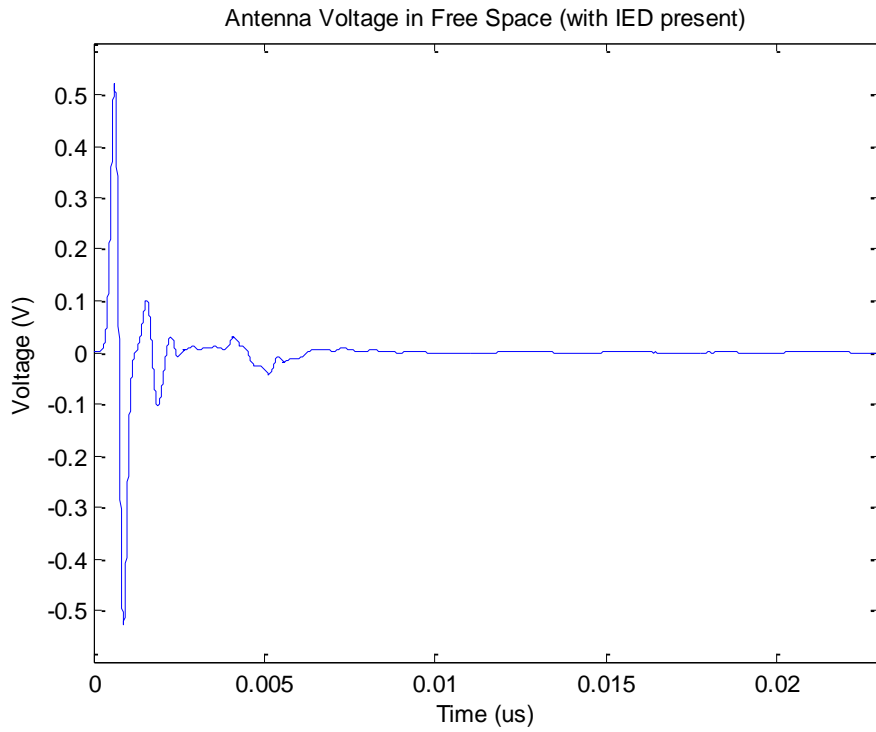
Figure 5.4. Antenna voltage in free space with an IED present.
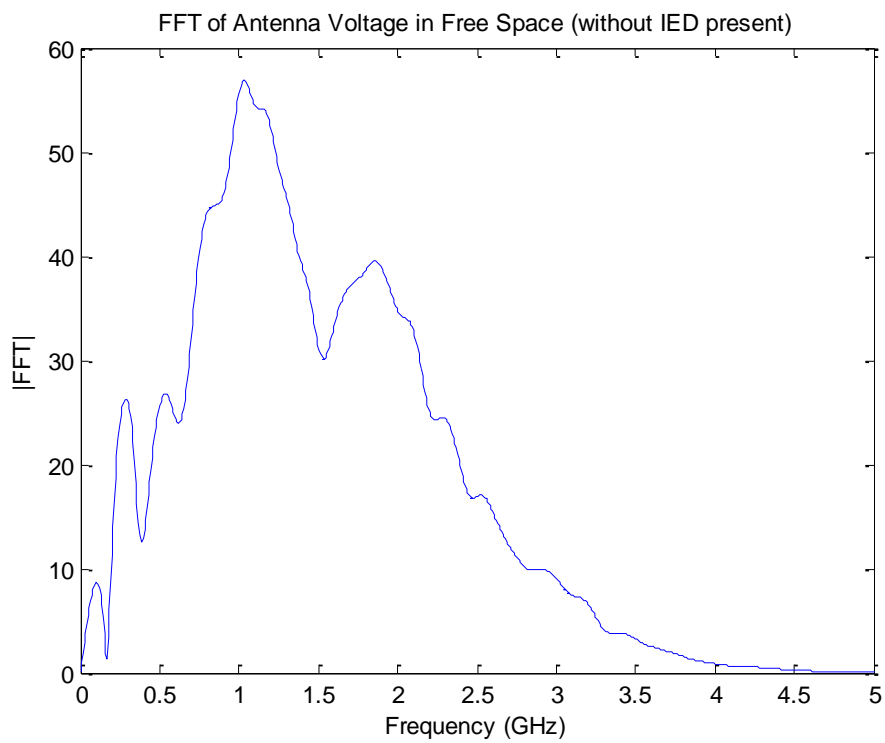
Figure 5.5. FFT of antenna voltage in free space without an IED present.
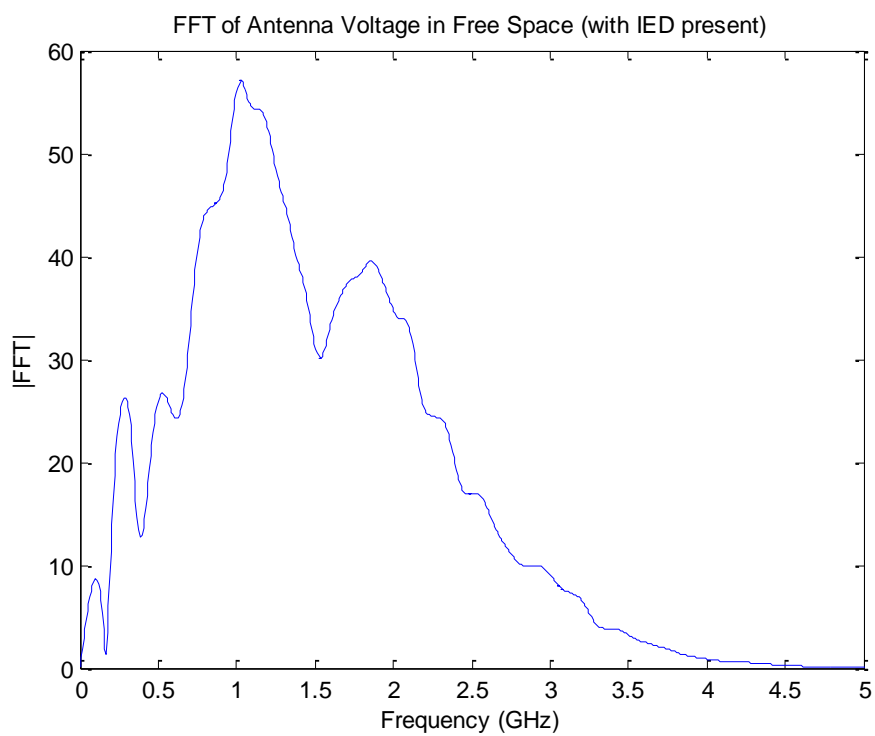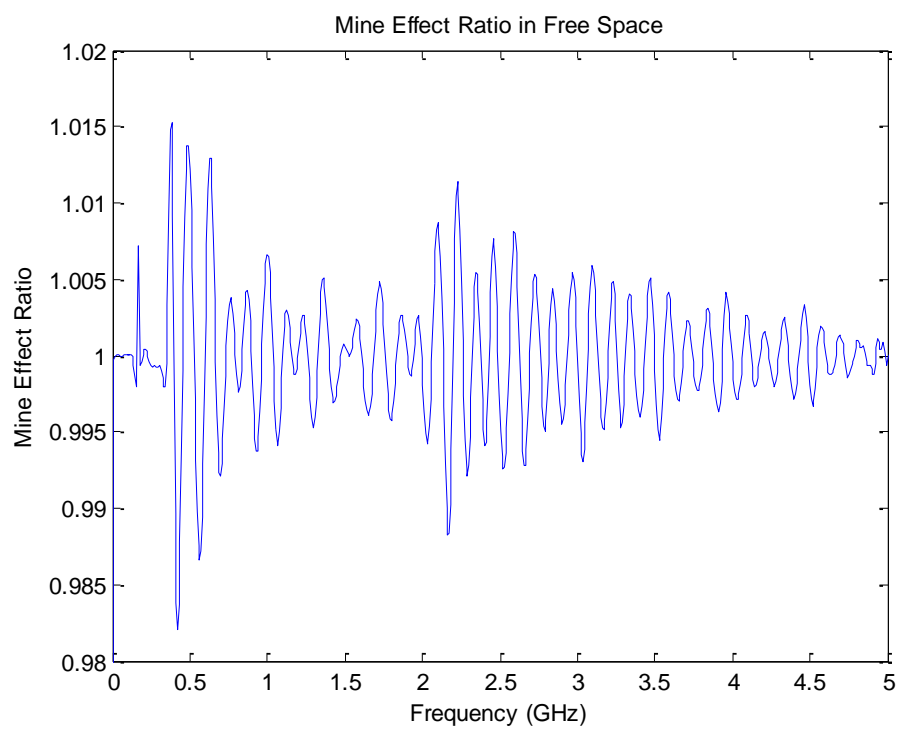
Figure 5.6. FFT of antenna voltage in free space with an IED present.

Figure 5.7. Mine effect ratio for free space.

Mine effect ratio in Figure 5.7 reveals two important characteristics of energy reflected from the VS-3.6. First, it is clear that its presence impacts the 0.3 – 0.8 GHz range significantly, as well as portions of spectrum between 2 and 3 GHz. This is likely a result of energy at resonant frequencies particular to such a large plastic mine reflecting back to the antenna. The presence of harmonics of the resonant frequency are possible explanations for the broad ranges of frequency effects found in Figure 5.7.

More interesting, however, is the periodic nature of free space's mine effect ratio. A potential explanation for this phenomenon lies in constructive and destructive interference. The mine itself is a large, singular object at some fixed distance from the antenna. As a result, every frequency component of the radar signal travels the same distance between the antenna and mine. Because wavelength differs between frequencies, traveling a fixed distance results in no phase shift for certain frequencies, partial phase shift for other frequencies, and complete 180 degree phase shift for yet other frequencies. When these reflections return to the antenna they combine, either constructively or destructively, with other signals of the same frequency already present in the antenna. Thus the presence of the mine appears to cause constructive interference at certain frequencies destructive interference at others; in reality, however, it adds to all frequency responses. Destructive interference is found at any point below a ratio of 1 in Figure 5.7 while constructive interference is any point above 1. This phenomenon is investigated more closely in section 5.5 of this chapter.

5.2. Homogeneous Flat Ground

Flat, homogeneous soil with $\varepsilon_r = 5$ and $\sigma = 0.05$ mS/m is tested. Figures 5.8 and 5.9 show the simulation environment and an electric field cutaway.
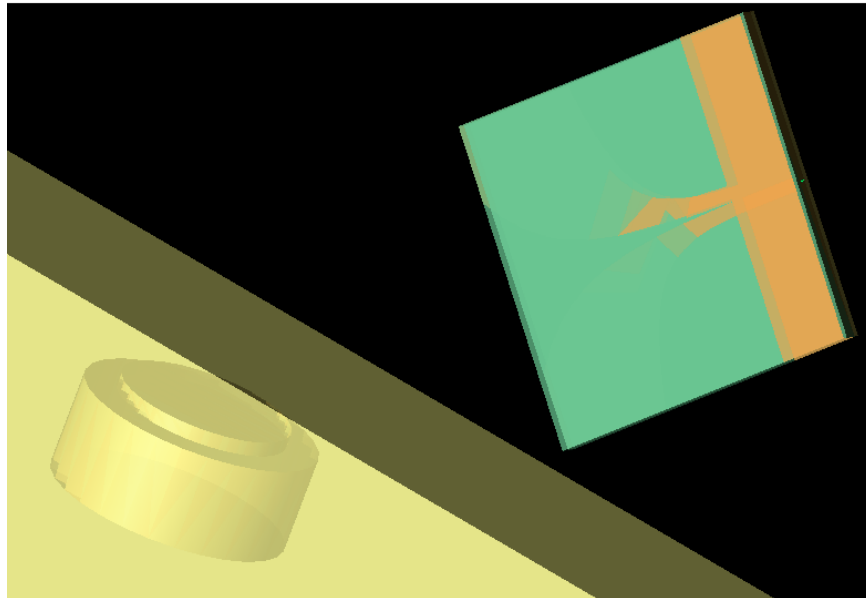
Figure 5.8. Screen capture of the XFdtd 7 GUI for the second run in homogeneous soil (68% opacity).
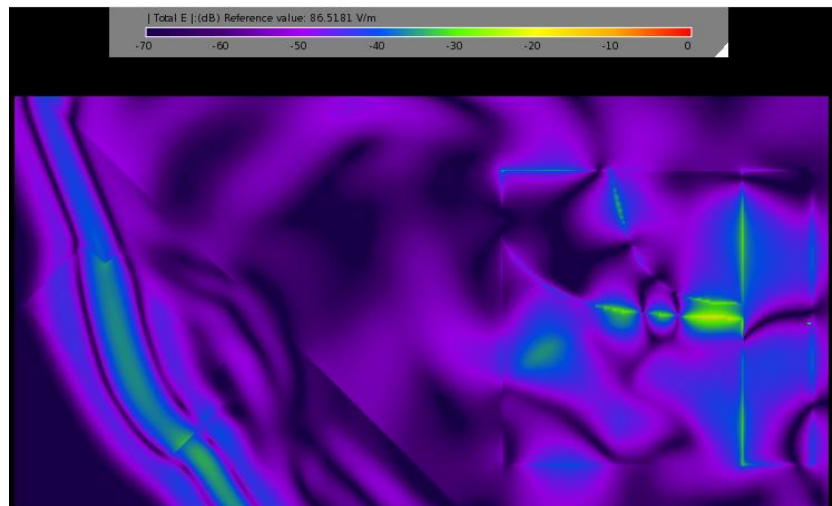

Figure 5.9. Screen capture of electric field propagation in 2-D, taken at time step 117; the antenna is to the right while the mine under the soil's surface is visible on the left.

Because, similar to the free space case, the time and frequency plots for both runs are almost identical, only the time and frequency data sets from the run with the target present are shown below in Figures 5.10 and 5.11.
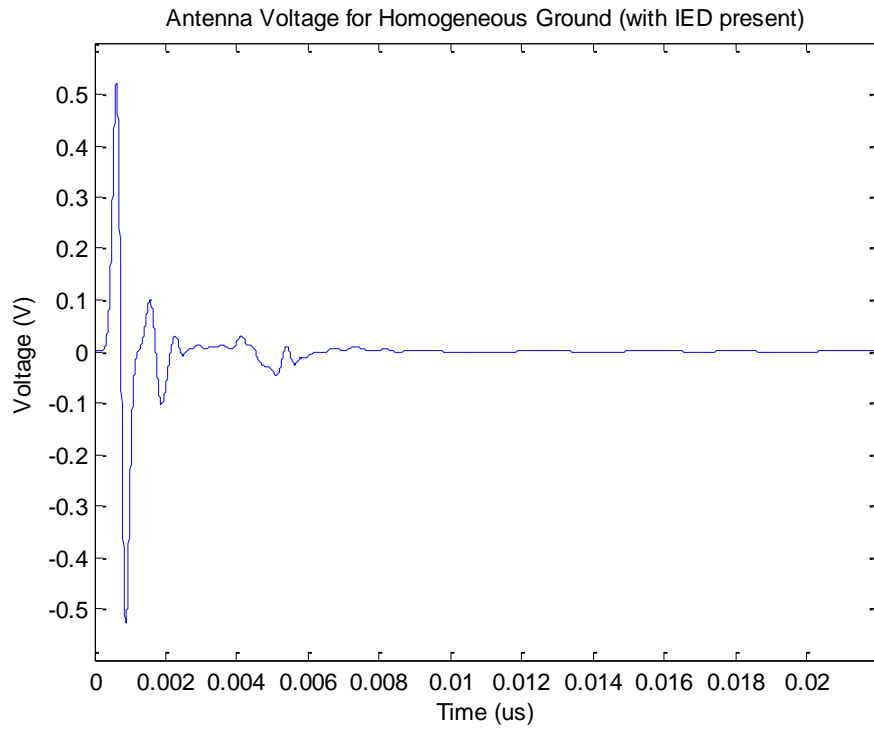
Figure 5.10. Antenna voltage for homogeneous ground with an IED present.
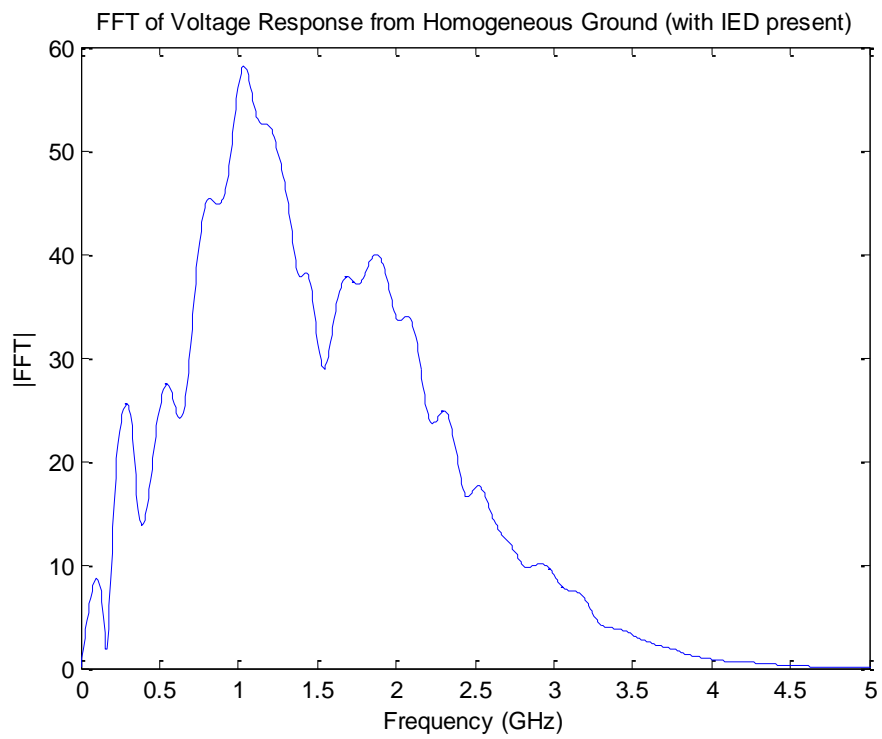
Figure 5.11. FFT of antenna voltage from homogeneous ground with an IED present.
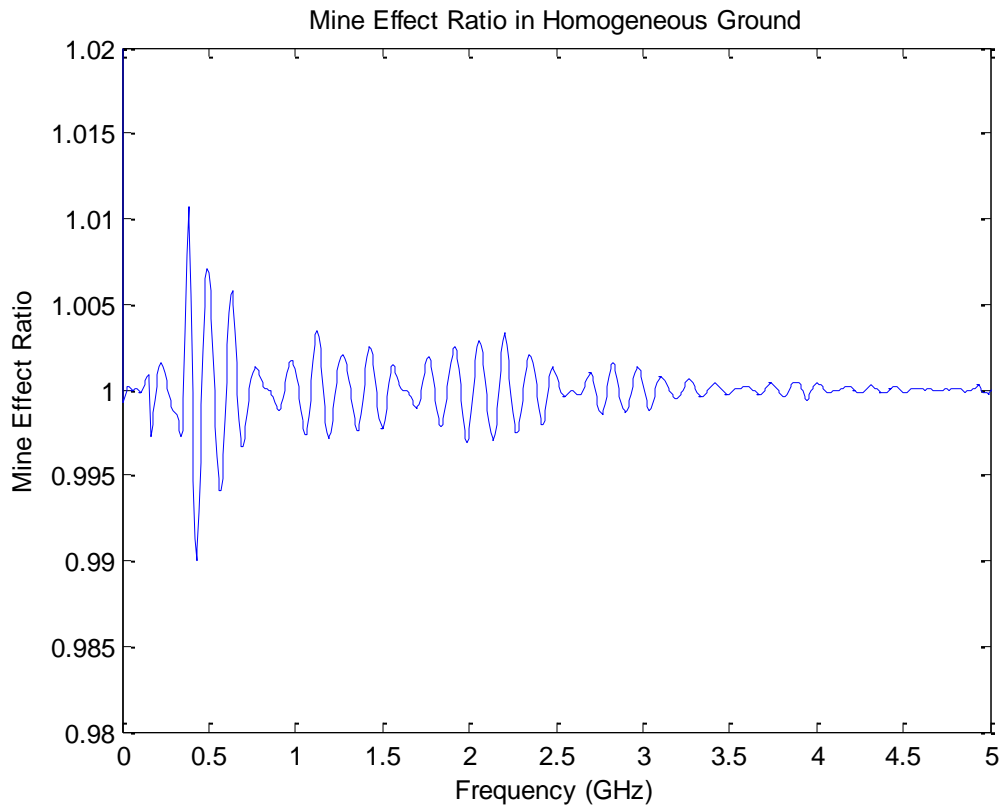
Figure 5.12. Mine effect ratio for homogeneous ground.

Figure 5.12 shows the mine effect ratio for homogeneous ground. Behavior here is very similar to that found in free space, exhibiting strong response at low frequencies and retaining the same periodic structure. The only significant difference between the free space and homogeneous ground cases, in terms of the target's frequency response, is found in mine effect ratio. The maximum amplitude of relative change found in Figure 5.12 is approximately 1.01, lower than the 1.016 found in Figure 5.7. This is a result of clutter reflections from the ground's surface combining with return energy from the mine. Because of this, the mine return signals now compete with clutter and are relatively diminished due to the net increase of total energy reflected back to the antenna.

5.3. Gravel Road

A gravel road is tested. Figures 5.13 and 5.14 show the simulation environment and an electric field cutaway.
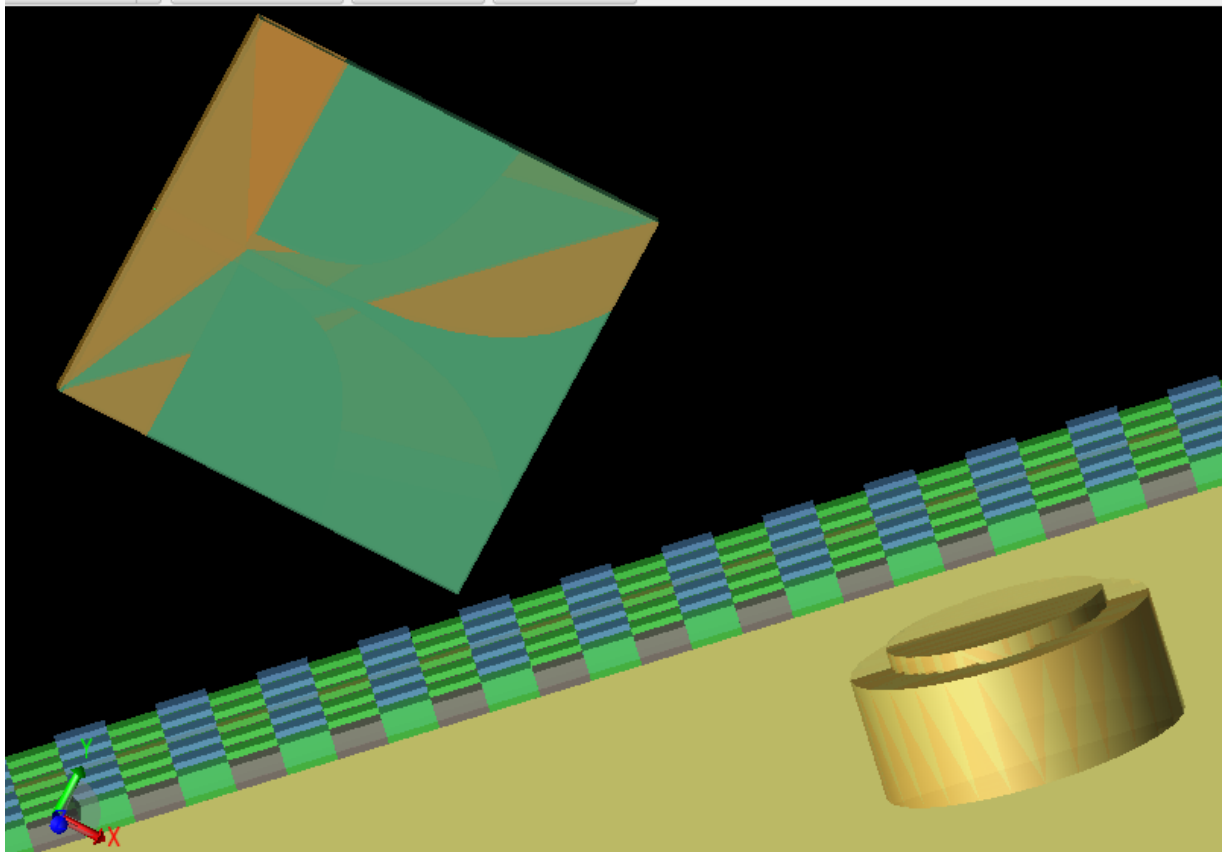

Figure 5.13. Screen capture of the XFdtd 7 GUI for the second run in a gravel road (70% opacity).

Here again, only the second set of time and frequency domain data is presented in Figures 5.15 and 5.16; Figure 5.17 follows with the mine effect ratio. As before, the diminished mine effect ratio maxima and minima result from increased clutter, due to the presence of gravel.
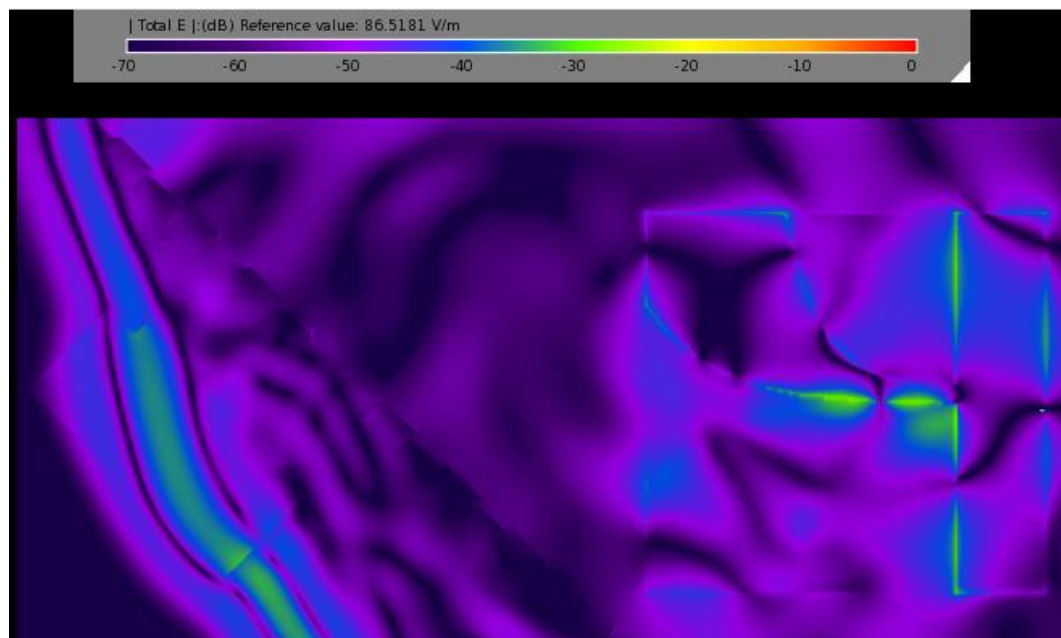
Figure 5.14. Screen capture of electric field propagation in 2-D, taken at time step 120; the antenna is to the right while the mine under the gravel road is visible on the left.
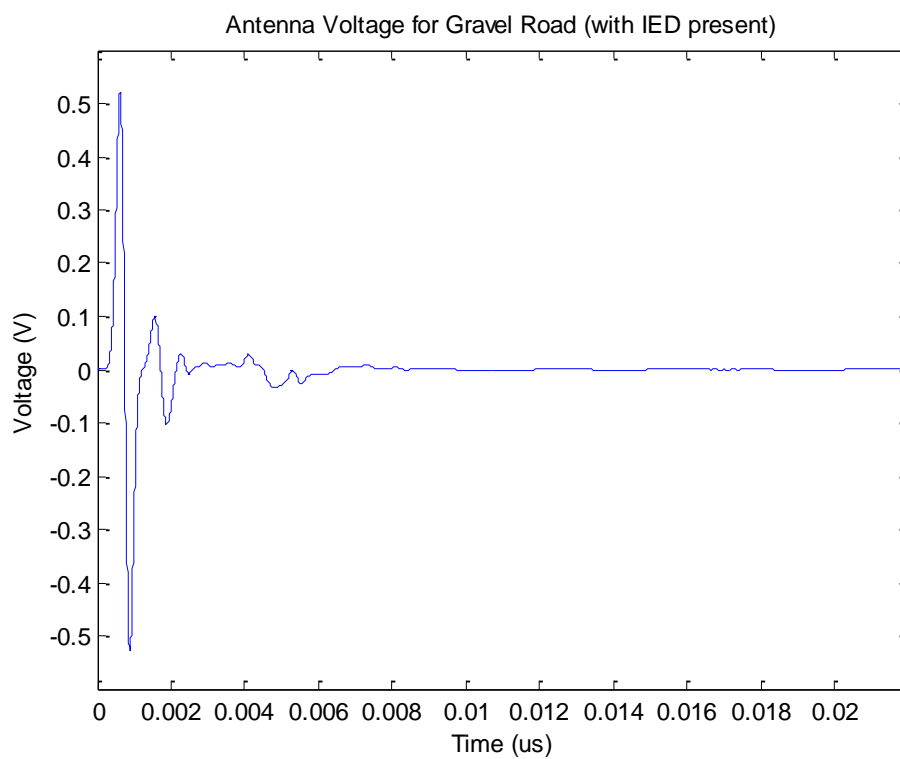

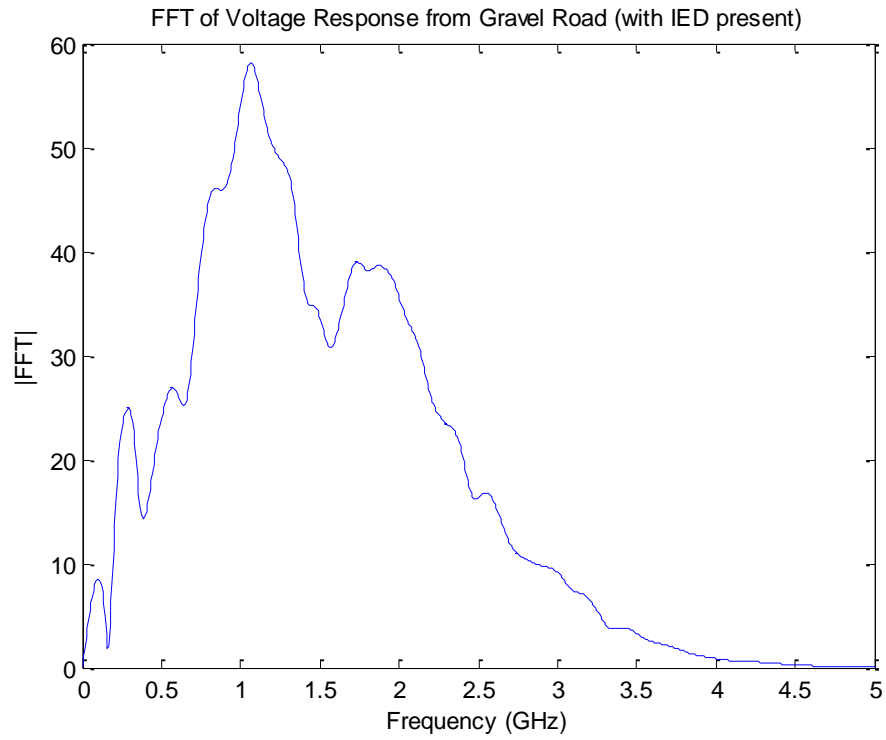**Figure 5.15. Antenna voltage for gravel road with an IED present.**

Figure 5.16. FFT of antenna voltage for gravel road with an IED present.
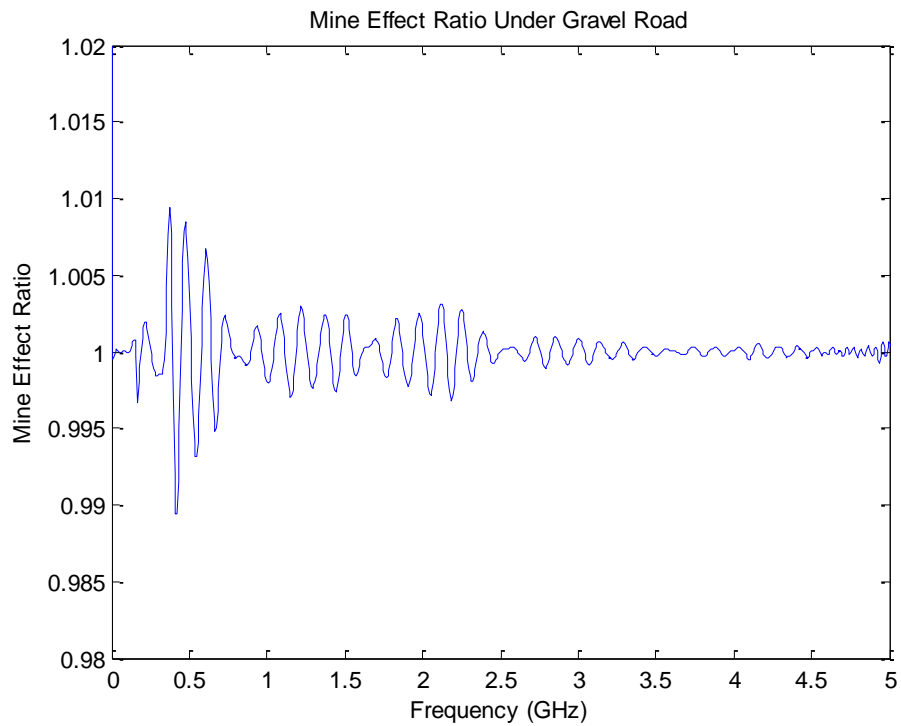

Figure 5.17. Mine effect ratio for a gravel road.

5.4. Rutted, Muddy Road with Shrapnel

In this final environment, a muddy gravel road with an oval rut is modeled. Three pieces of metallic shrapnel are buried a few centimeters above the mine. Figure 5.18 shows an image of the simulation space and Figure 5.19 presents a cutaway of electric field propagation through the environment.
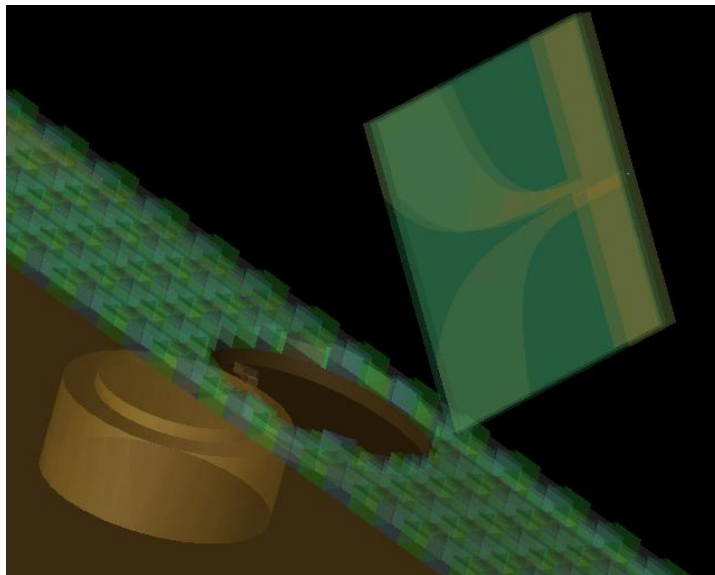

Figure 5.18. Screen capture of the XFdtd 7 GUI for the second run in a rutted road (20% opacity).
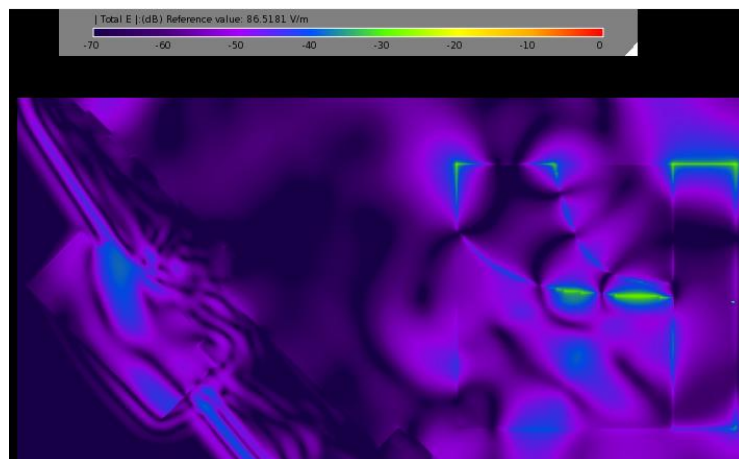

Figure 5.19. Screen capture of electric field propagation in 2-D, taken at time step 133; the antenna is to the right while the mine under the gravel road is visible on the left.

Finally, one set each of the time and frequency data is shown below in Figures 5.20 and
5.21. Mine effect ratio follows in Figure 5.22. Its behavior mimics the previous cluttered cases.
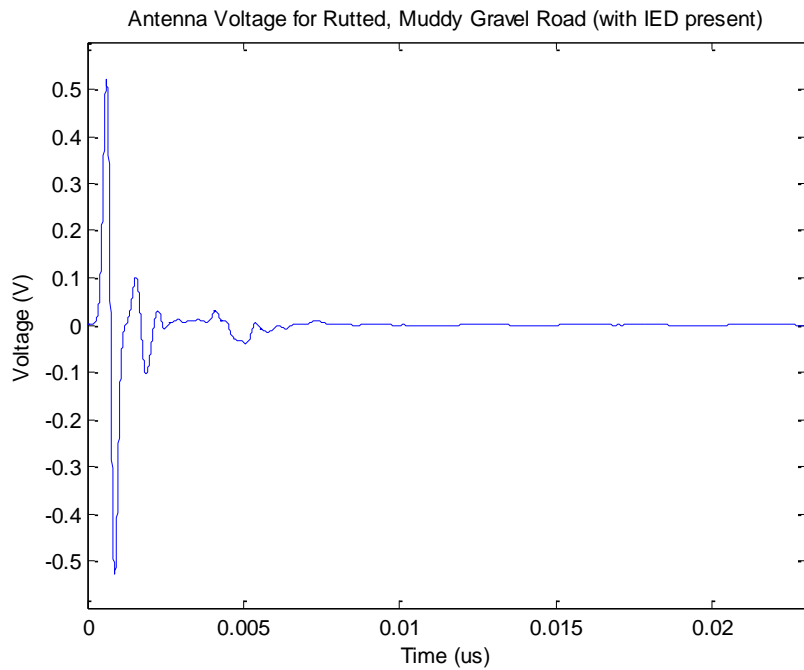

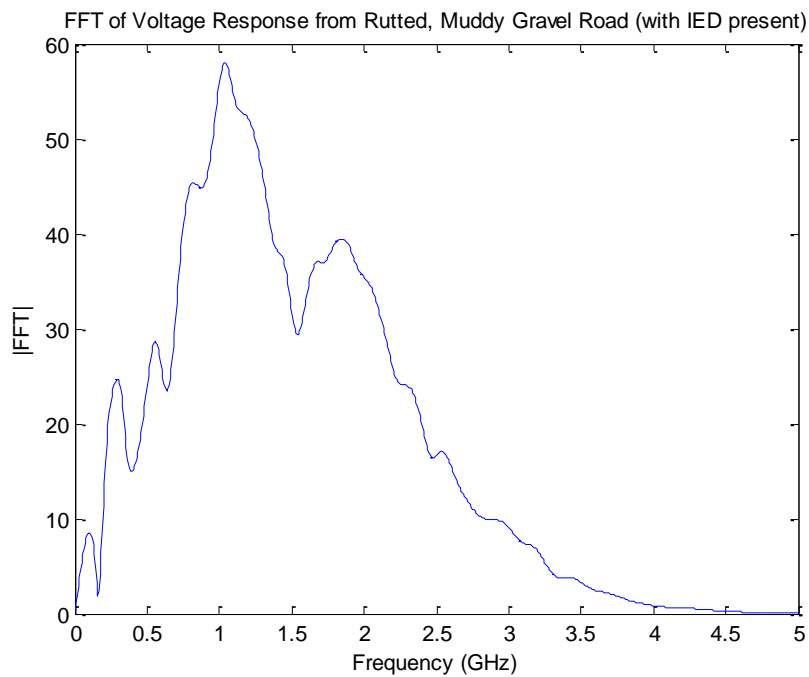**Figure 5.20. Antenna voltage for rutted road with an IED present.**

Figure 5.21. FFT of antenna voltage for rutted road with an IED present.
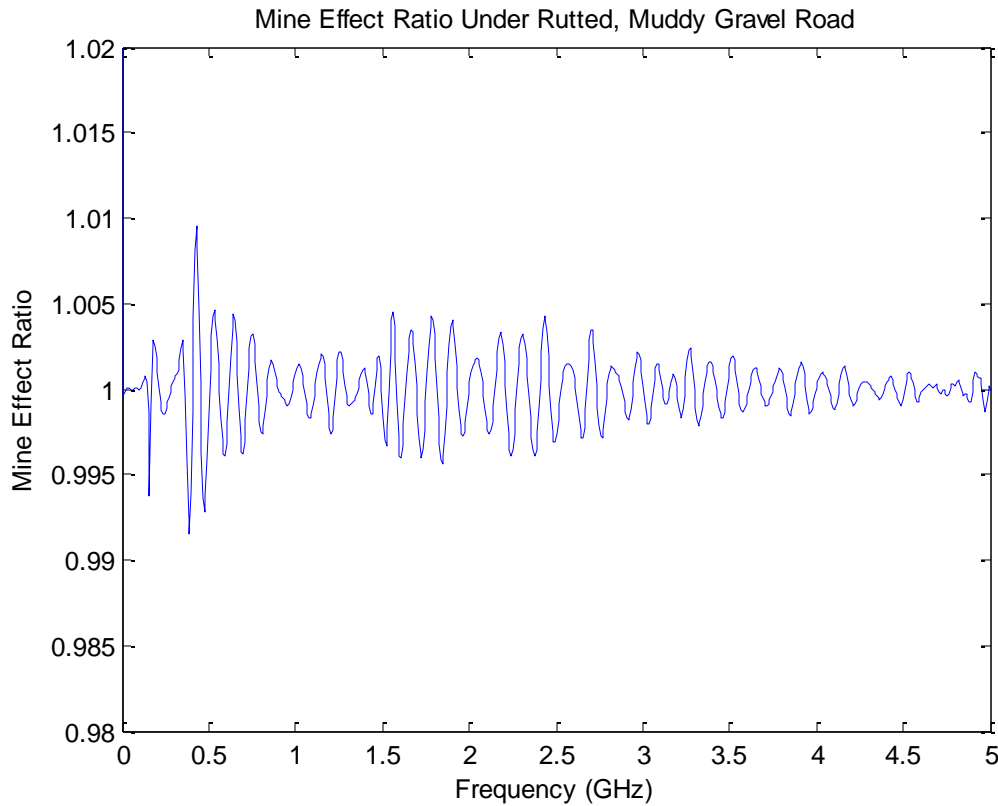
Figure 5.22. Mine effect ratio for a rutted road.

It is important to note that all graphs of mine effect ratio above share a few common features. First, each case shows most significant change at low frequencies between $0.3 - 0.8$ GHz. Second, the approximate periodicity is shared between every graph, with an average of approximately 32 peaks in the $1 - 5$ GHz range.

5.5. Clutter Effect Ratio

In every case above, mine effect ratio exhibits periodicity. Clutter, on the other hand, is often random and unpredictable. It may be possible to extract the periodicity of mine effect ratio from data with both clutter and a mine present. First, the randomness of clutter effect ratio must be confirmed; to do this, a ground truth is chosen. Ground truth serves as the most ideal

environment against which all others are compared. Ground truth has no, or at least a reasonably

low amount of, clutter present. In this case, the frequency results from the homogeneous ground

environment, without a mine, are chosen as ground truth. Next, frequency data from an

environment with significantly more clutter, also without a mine, are divided by the ground truth.

This process is identical to that which determines mine effect ratio; it is now called clutter effect

ratio. Figures 5.23 and 5.24 show clutter effect ratio for gravel and rutted, muddy roads,
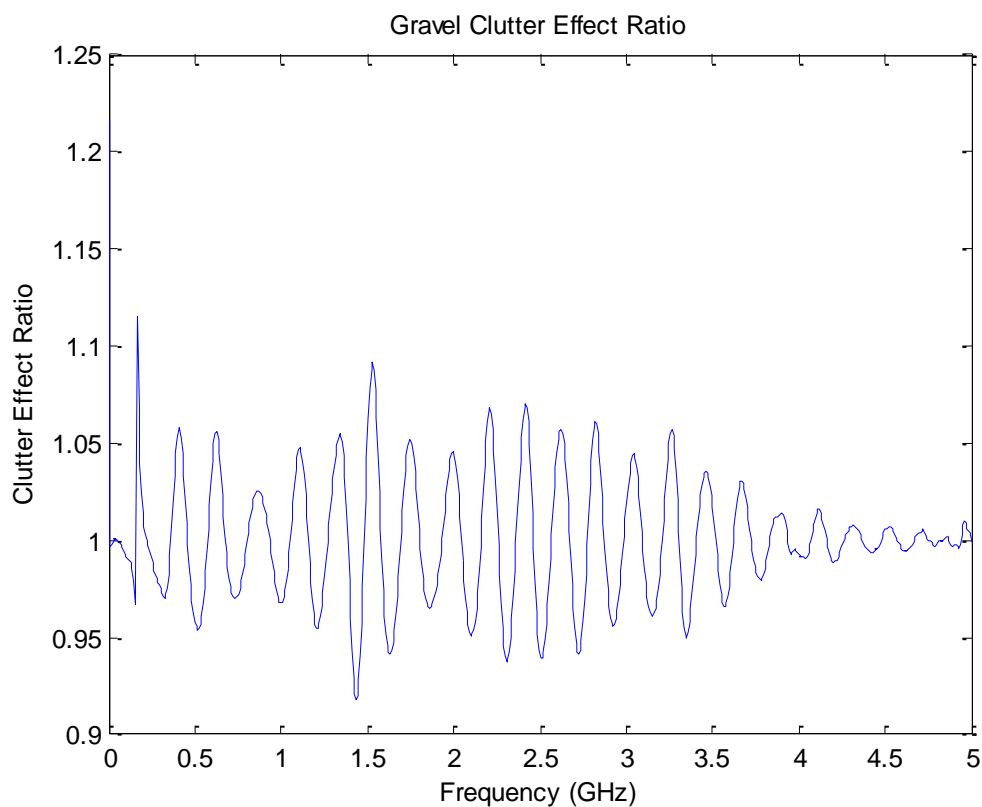
respectively.

Figure 5.23. Clutter effect ratio for a gravel road.

Unfortunately, both clutter effect ratios exhibit significant periodicity. Portions of low

frequency content in Figure 5.24 are semi-random, but the effect of clutter on FLGPR

measurement simulations here is not nearly as random as expected.

A possible explanation for the periodicity of clutter response is simulation inaccuracy. For the sake of time conservation and simplicity, the gravel case was modeled with a pattern tool in XFdtd7. Figure 4.3 shows that it even has some axes of symmetry. Lack of true randomness may cause periodic clutter effect ratio for a gravel road. The rutted, muddy road with shrapnel is more random, but still based on the original gravel road model. As a result, the slight increase of randomness from Figures 5.23 to 5.24 may be a product of the slight increase of randomness from the gravel road model to the rutted, muddy road with shrapnel model. The results shown above do not prove that clutter's effect isn't random. In fact, most researchers agree that the effect of clutter on GPR measurements is completely random. This is convincing evidence that clutter has not been modeled properly here.
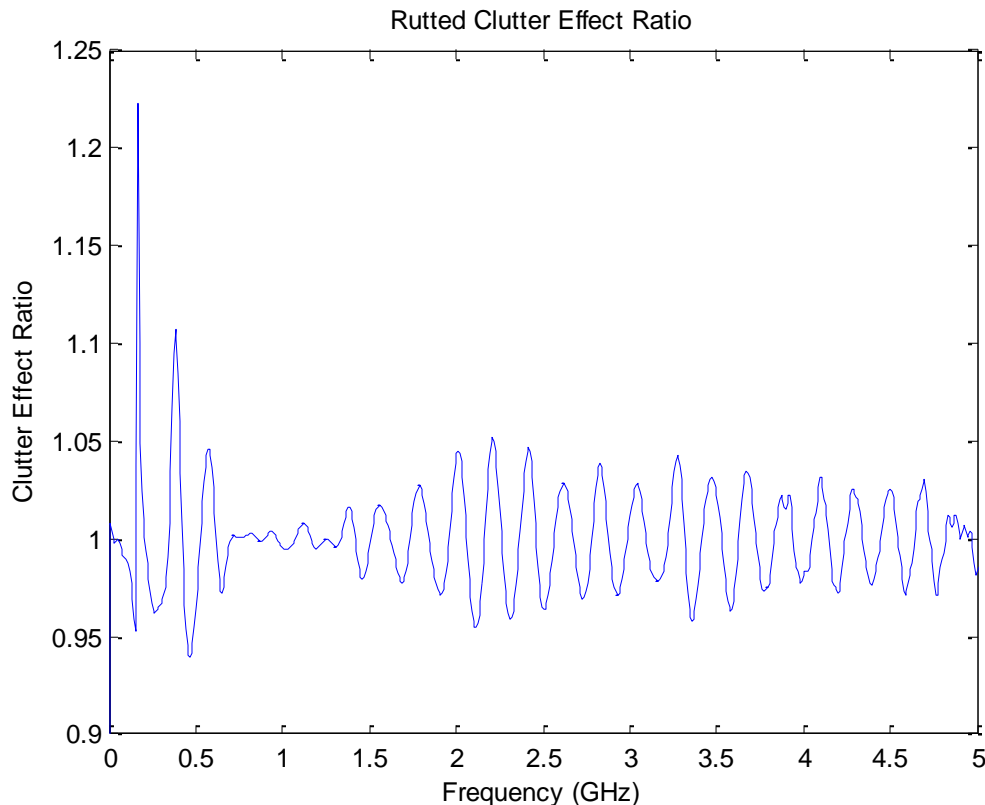

Figure 5.24. Clutter effect ratio for a rutted, muddy road.

To verify the periodicities found in the clutter effect ratio, FFTs of Figures 5.23 and 5.24 are evaluated and shown in Figures 5.25 and 5.26. The units on the resulting axes are unknown and of little consequence for the general observations made here. There are five noticeable peaks. The peaks on the far left and far right stand significantly higher than the middle three for both graphs, and all five peaks fall at the same locations between data sets. These results indicate that the clutter effect ratios, as shown above, exhibit periodicity at five main rates and verify that which was assumed earlier by the naked eye.
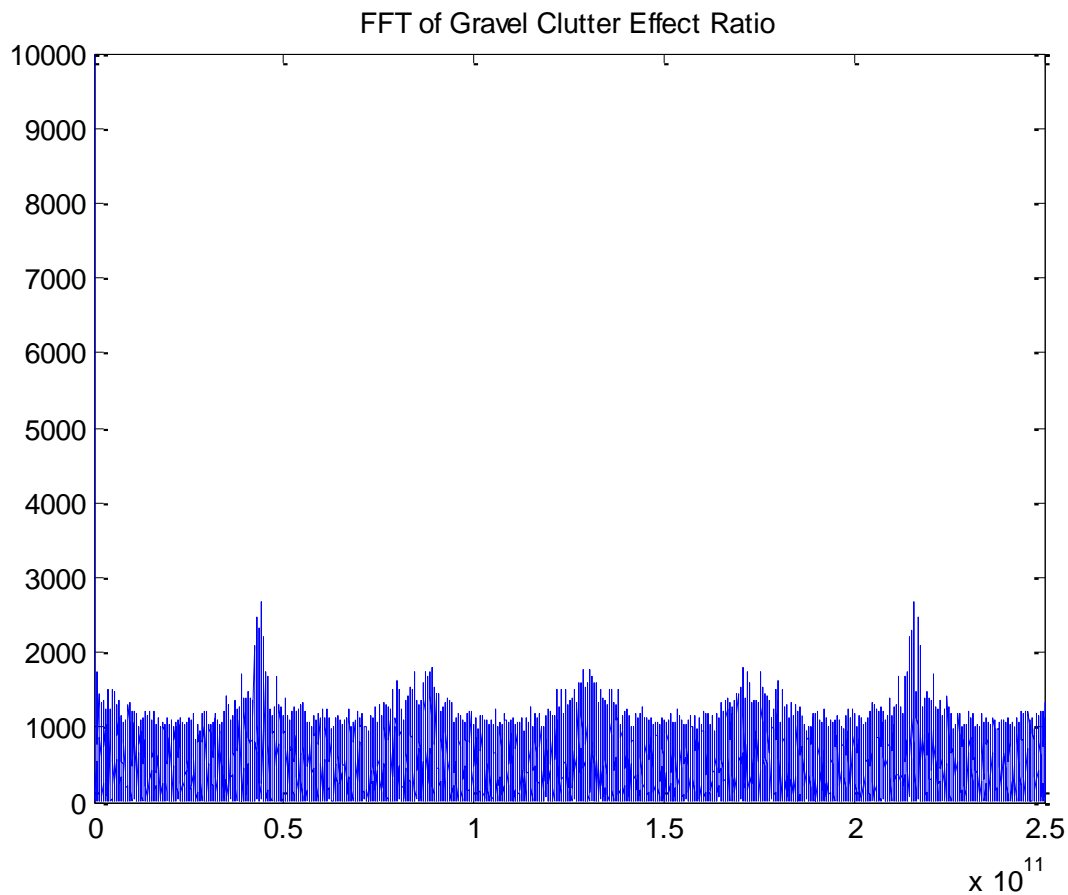

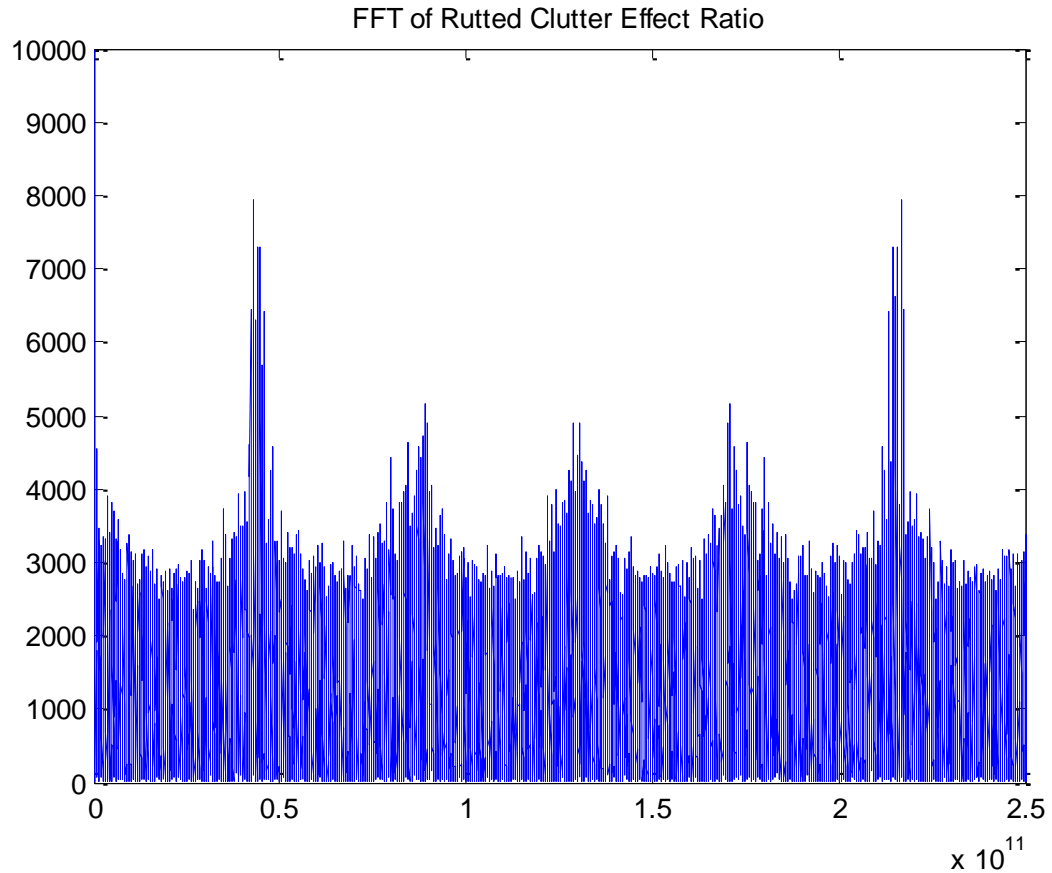**Figure 5.25 FFT of gravel clutter effect ratio.**

Figure 5.26 FFT of rutted road clutter effect ratio.

Specular reflections from the ground are likely additional factors contributing to the periodicity found in clutter effect ratio. As with a mine, the ground as a whole may be causing periodic reflections that cancel constructively and destructively with energy in the antenna. In order to determine if the ground is the cause of the specular reflections, free space is now chosen as ground truth, and the simplest environment, homogeneous soil, is used to generate a new clutter effect ratio (Fig. 5.27). This clutter effect ratio is more of a ground effect ratio; it shows the difference caused by adding flat soil to the free space case.
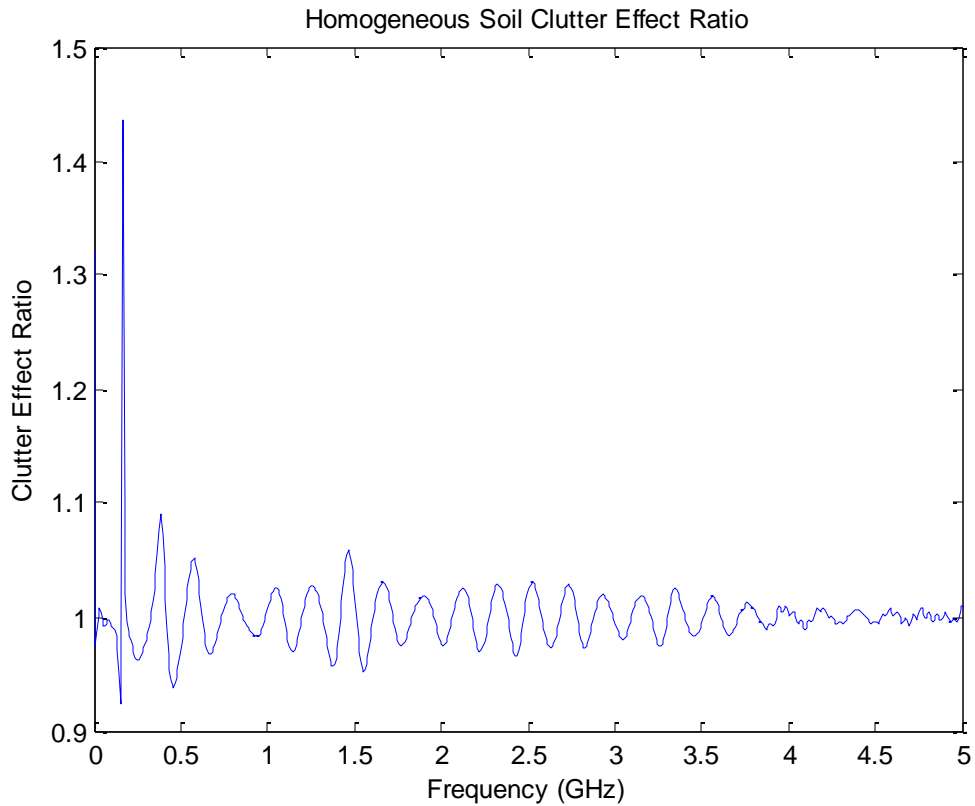
Homogeneous Soil Clutter Effect Ratio

Figure 5.27. Homogeneous soil clutter effect ratio.

Figure 5.27 is strong evidence that the specular reflections found in clutter effect ratios calculated here are caused by the ground itself and not clutter. Though the model used for clutter is still incorrect, this data points to other methods of extracting the presence of a mine from frequency domain data. The specular reflections from the ground exhibit a periodicity of approximately 20 peaks through the $1 - 5$ GHz range while mine effect ratio's periodicity has nearly 33 peaks in that same range. Thus, the higher frequency specular reflections caused by the presence of a mine may be a detectable quantity and an indicator of a mine's presence.

Chapter 6: Conclusion

FLGPR is an effective system capable of detecting 100% of buried explosives, including plastic mines, 100% of the time. Its greatest weakness lies in the cost of guaranteed target detection; FLGPR results often include a significant number of false alarms. Of great value, then, is research focusing on methods of reducing the false alarm rate of FLGPR systems.

Mine effect ratio measurements in Chapter 5 agree with results found in [5]. The effect of adding a VS-3.6 mine to an environment is most significant at low frequencies. In the cases investigated, mine effects were most noticeable from 0.3 to 0.8 GHz. The frequency based classifier discussed in [5] appears to be an effective method of lowering false alarm rate when detecting low metal content plastic mines.

In addition, specular reflections from both the ground and mine are observed. Though the presence of ground and clutter contribute reflections of larger amplitude than those of a mine, they occur at different frequencies. It may be possible to extract the high frequency of a mine's weak specular reflections from the low frequency of the ground's strong specular reflections, and thus detect the presence of a buried explosive.

Follow-up to this work could involve validating or disproving these results. Better models of random clutter need to be developed to assess whether or not clutter effect response is periodic or if it is, in fact, random. In addition, specular reflections from buried targets and the ground itself warrant further investigation, as they represent another possible method of distinguishing between a mine and its cluttered surroundings. From there, research into the frequency domain effects of a mine's presence can continue forward, searching for a method of distinguishing between the frequency domain effects of clutter and those of a buried IED.

Bibliography

[1]   Jol, Harry M. *Ground Penetrating Radar: Theory and Applications*. Amsterdam: Elsevier Science, 2009. Print.

[2]   Wong, D., Tuan Ton, and M. Soumekh. "ALARIC Forward-Looking Ground Penetrating Radar System with Standoff Capability." *2010 IEEE National Conference on Wireless Information Technology and Systems*, pg. 1, 2010.

[3]   Youn, Hyoung-sun, J. Kobashigawa, M. Evans, and N. Celik. "Feasibility Study for IED Detection Using Forward-Looking Ground Penetrating Radar Integrated with Target Features Classification." *2010 IEEE Antennas and Propagation Society International Symposium*, pg. 1, 2010.

[4]   Sun, Y., and J. Li. "Time-Frequency Analysis for Plastic Landmine Detection via Forward-Looking Ground Penetrating Radar." *IEEE Proceedings on Radar, Sonar and Navigation,* vol. 150, no. 4, pp. 253-61, 2003.

[5]   Wang, Tsaipei, James M. Keller, Paul D. Gader, and Ozy Sjahputera. "Frequency Subband Processing and Feature Analysis of Forward-Looking Ground-Penetrating Radar Signals for Land-Mine Detection." *IEEE Transactions on Geoscience and Remote Sensing*, vol. 45, no. 3, pp. 718-29, 2007.

[6]   Ho, K.C., L. Carin, and P.D. Gader. "An Investigation of Using the Spectral Characteristics From Ground Penetrating Radar for Landmine/Clutter Discrimination." *IEEE Transactions on Geoscience and Remote Sensing,* vol. 46, no. 4, pp. 1177-1191, 2008.

[7]   Rappaport, C.M. "Soil Moisture and Surface Roughness Effects in Ground Penetrating Radar Detection of Land Mines." *IEEE MTT-S International Microwave Symposium Digest,* pg. 180, 2006.

[8] Ortega, R., and Chi-Chih Chen. "FDTD Modeling of Scattering from Distant Buried Objects." *2007 IEEE Antennas and Propagation Society International Symposium*, 2007.

[9] Balsi, M., S. Esposito, F. Frezza, and P. Nocito. "GPR Measurements and FDTD Simulations for Landmine Detection." *2010 13th International Conference on Ground Penetrating Radar (GPR)* (2010): 1. Print.

[10] Ulaby, Fawwaz Tayssir. *Fundamentals of Applied Electromagnetics*. 5th ed. Upper Saddle River, NJ: Pearson Prentice Hall, 2007. Print.

[11] Balanis, Constantine A. *Modern Antenna Handbook*. Hoboken, NJ: J. Wiley & Sons, 2008. Print.

[12] Kunz, Karl S., and Raymond J. Luebbers. *The Finite Difference Time Domain Method for Electromagnetics*. Boca Raton: CRC, 1993. Print.

[13] Yee, Kane. "Numerical solution of initial boundary value problems involving Maxwell's equations in isotropic media". *IEEE Transactions on Antennas and Propagation*, vol. 14, no. 3, pp. 302–307, 1966.

[14] Jean-Pierre Berenger. "A Perfectly Matched Layer for the Absorption of Electromagnetic Waves," *Journal of Computational Physics*, vol. 114, pp. 185-200, 1994.

[15] *Global Terrorism Database*. University of Maryland, 2009. Web. 9 Apr. 2011. <http://www.start.umd.edu/gtd/>.

[16] "Soil Regions Map of Afghanistan." *Natural Resources Conservation Service: Soils*. United States Department of Agriculture, 21 Sept. 2005. Web. 09 Apr. 2011. <http://soils.usda.gov/use/worldsoils/mapindex/afghanistan-soil.html>.

[17] "Afghanistan." *Encyclopedia Britannica Online*. Encyclopedia Britannica. Web. 9 Apr. 2011. <http://www.britannica.com/EBchecked/topic/7798/Afghanistan/21418/Climate>.

[18] "VS-N Fuzed Mines." *Wikipedia, the Free Encyclopedia*. 26 Dec. 2010. Web. 09 Apr. 2011.

<http://en.wikipedia.org/wiki/VS-N_fuzed_mines>.

[19] Shin, Joon, Schaubert, D.H. "A Parameter Study of Stripline-fed Vivaldi Notch-Antenna Arrays". *IEEE Transactions on Antennas and Propagation*, vol. 47, no. 5, pp. 879-886, 1999.

[20] Gibson, P.J. "The Vivaldi Aerial". *9th European Microwave Conference*, pg. 101, 1979.